ORIGINAL ARTICLE

Biogenic synthesis of silver anchored ZnO nanorods as nano catalyst for organic transformation reactions and dye degradation

Omkar S. Karvekar[1] · Prashant D. Sarvalkar[1] · Apurva S. Vadanagekar[1] · Richa D. Singhan[1] · Sarita M. Jadhav[1] · Mansingraj S. Nimbalkar[2] · Neeraj R. Prasad[1]

Abstract

In this study, we are reporting biogenic synthesis of silver nanoparticles and hydrothermal synthesis of zinc oxide nanoparticles. Using convenient mechanical milling methods, nanocomposites with superior photocatalytic and catalytic properties are synthesized. Herein, we have adopted a green, eco-friendly, and economical route for the synthesis of Ag nanoparticles using Zingiber officinalae rhizome extract in an aqueous solution. The synthesized materials were characterized using UV–Vis spectroscopy, XRD, SEM & FE-SEM, FT-IR, Raman, and a particle size analyzer with zeta potential analysis. The photocatalytic activities of Ag, ZnO and their composites were studied by observing the degradation of methylene blue and crystal violet dyes under natural sunlight. Then the catalytic efficacies of synthesized nanoparticles for various organic transformation reactions were studied. Ag–ZnO nanocomposites were predicted to have improved photocatalytic activity and organic transformation reactions, allowing them to be used in environmental remediation applications.

Keywords Ag NPs and ZnO nanorods · Composite nanomaterials · Organic transformation · Dye degradation · Nanocatalysis

Introduction

Today nanomaterials are used in almost every sector of science and technology to improve human lives and the environment in numerous ways. The first evidence of a link between human life and the nanoscale is probably can be found in Ayurveda, which is a 5000-year-old Indian system of medicine. Even before the term nanotechnology was invented, Ayurveda had some understanding of nanomedicine manufacturing and their effects (Prasad and Elumalai 2011; Prasad et al. 2021). The creation of metallic nanoparticles (NPs) is well documented in the ancient Ayurvedic literature, Ras-Ratnakar (Nazeruddin et al. 2014). Nanomaterials have features that are substantially distinct from bulk

counterparts at the nanoscale, and they can be employed in solar cells, lithium ion batteries, bio-sensors, gas sensors, memristors, transistors, in smart textiles, veterinary medicines or as catalysts for chemical transformation reactions (Mahdieh et al. 2012). Because metal NPs are biocompatible and employed in water purification, catalysis, and other applications, there has been a lot of interest in developing approaches for the controlled synthesis of metal NPs with well-defined shapes, sizes, and compositions (Khan et al. 2012).

When discussing the causes of water pollution in conventional sectors, the use of non-green chemicals in manufacturing comes up (Liao et al. 2021). Hazardous slurries are employed in traditional industries to manufacture or polish high-performance devices, which are commonly used in the semiconductor, microelectronics, and aerospace industries (Zhang and Su 2020). To address this issue, green synthesis nanoparticles, nanomaterials, and nanotechnology are being used to develop new green slurries (Zhang and Su 2020), diamond wheels(Zhang et al. 2017), and machining processes(Zhang et al. 2015) that will be used to find alternative green products in industries. High-performance surfaces are created using developed slurries, equipment and

✉ Prashant D. Sarvalkar
   prashantsarvalkar22@gmail.com

✉ Neeraj R. Prasad
   neeraj_prasad21@rediffmail.com

1   School of Nanoscience and Technology, Shivaji University, Kolhapur 416004, Maharashtra, India

2   Department of Botany, Shivaji University, Kolhapur 416004, Maharashtra, India

processes that are exceptionally challenging to construct in traditional industries (Zhenyu et al. 2012). Nevertheless, these studies are a watershed moment for traditional industries and dramatically lower pollution levels in the environment. (Cui et al. 2019; Zhang et al. 2022).

The presence of carbonyl groups found in aspartic acid and/or glutamine residues, as well as the hydroxyl residues of proteins, is believed to be a viable reaction center for the creation of NPs using plant extracts. One of the goals of employing plant extracts was to establish a quick synthesis of NPs that took only a few hours, as opposed to the traditional biosynthetic method involving microorganisms, which takes 2–4 days to completely reduce metal ions. Few medicinal plants are known to have antioxidant properties, which means they can operate as a biological supply of reducing agents. The properties of material at nanoscale depends upon their size and shape. The size and shape of the particles are influenced by various factors such as concentration of solution, pH, reaction temperature, nature of reducing agent and capping agents and time of contact. The considerable work in the domain of biogenic synthesis of transition metal nanomaterials were done by S. Shiv Shankar (Shankar et al. 2004). The manufacture of Ag and Au NPs using *Azadirachata indica* decoction solution was reported by S. Shiv Shankar et al. The NPs, are in the 50–100 nm range and are not well separated from one another (Shankar et al. 2004).

In-vitro biogenic fabrication of materials at nanoscale is a promising topic for biodiversity-rich countries like India, in particular. Biodiversity can thus be leveraged as a valuable resource for biotechnological products and processes, including large-scale production of NPs of various sizes and forms (Ahmad et al. 2010). Herein, an attempt has been made for extra cellular bio-synthesis of transition metal NPs using ginger rhizome extracts. In a tropical country like India, *Zingiber officinale*, which belongs to the *Zingiberaceae* family, is a widely available herb that is extensively utilized in Indian cuisine. It's been used for centuries to cure bronchitis, carminative, hypertension, migraines, and other diseases. Apart from this during the recent pandemic situation of Covid-19, ginger was highly recommended from Ayurvedic doctors. This plant's rhizome extract is known to have diuretic qualities and is used as a cleaner and analgesic agent in ear drops. In comparison to aspirin, this plant is also used to enhance appetite and cure asthma, and it is thought to be a possible anti-platelet agent. It has anti-inflammatory and analgesic qualities similar to non-steroid anti-inflammatory medications, but without the gastrointestinal bleeding and ulcer development adverse effects (Pawar et al. 2015). The rhizome extract of *Zingiber officinale* is utilized here as a reducing and stabilizing agent. As a result, this process is both environmentally friendly and cost-effective when compared to other methods of synthesis. Protein in the aqueous extract could function as a bio-ligand. This approach

synthesized NPs that were well dispersed and showed no signs of aggregation.

Experimental section

Materials

Zinc nitrate hexahydrate ($Zn(NO_3)_2 \cdot 6H_2O$), 30 wt% Ammonia solution, Silver nitrate ($AgNO_3$), Methylene Blue (MB) and Crystal Violet (CV) dye, Analytical grade 4-Nitrophenol ($C_6H_5NO_3$) (4-NP), 2-Nitroaniline ($C_6H_6N_2O_2$) (2-NA), 3-Nitroaniline ($C_6H_6N_2O_2$) (3-NA), 4-Nitroaniline ($C_6H_6N_2O_2$) (4-NA), and Sodium Borohydride ($NaBH_4$) chemicals are procured form Sigma-Aldrich, Milwaukee (USA). The fresh Zingiber officinale rhizome is procured from the local market in India (N-16.67.35, E-74.25.32).

Bio-genic synthesis of Ag nanoparticles (NPs)

To prepare the extract, 10 g of rhizome was taken and properly cleansed in running tap water followed by distilled water so as to remove any foreign material adhered to the surface. Then the rhizome was macerated overnight in 100 mL of double distilled water. It was then coarsely crushed in a grinder mixer, filtered with absorbent cotton, and the filtrate was stored in a stoppered glass bottle. The extracted solution was stored at a 4 °C temperature in the refrigerator for further use.

A 250 mL beaker was filled with 100 mL of 0.1 M AgNO₃ solution. Then, in the burette, 50 mL of *Zingiber officinale* rhizome extract was filled and dropwise added with constant stirring into the beaker containing the AgNO₃ solution. During the biosynthesis process we maintained normal room temperature and pressure. After the addition of a sufficient amount of rhizome extract to the beaker containing AgNO₃ solution, we observed a black coloured precipitate in the reaction mixture. This black-coloured precipitate can be separated from the reaction mixture using high-speed centrifugation operating at 5000 rpm. To eliminate organic contaminants soluble in alcohol, the separated precipitate was washed twice with ethanol. The black coloured solid mass was kept in the oven for drying at 60 °C. The entire drying process produced a black coloured substance, which was ground in a mortar-pestle and sampled for characterization.

### Mechanism of biosynthesis of metallic NPs

The synthesis of Ag NPs by biological entities is due to the presence of a large number of organic chemicals like carbohydrates, fats, proteins, enzymes, coenzymes, phenols, flavonoids and alkaloids. The literature survey reveals that the primary components of *Zingiber officinale* include gingerol,

shogaol, regin, and starch. As a result, the plant rhizome extract can act as a reducing agent and a capping agent, preventing the NPs from agglomeration (Yeh et al. 2014). The synthesis of Ag NPs is the result of the reduction of Ag$^+$ ions, which is followed by agglomeration into oligomeric clusters. These clusters eventually result in the creation of colloidal Ag particles with nanometer-sized dimensions. The solution displays a black colour with a prominent band in the 370–440 nm range and other less strong or smaller bands at a longer wavelength in the UV–Vis absorption spectrum.

The active ingredient responsible for the reduction of Ag$^+$ ions varies depending upon the extract used. For nano-During transformation of Ag$^+$ into Ag NPs, electrons are supposed to be derived from dehydrogenation of acids (ascorbic acid) and alcohols (catechol) in hydrophytes, Keto to Enol conversions (paraquinone, dietchequinone, remain) in mesophytes or both mechanisms in xerophytic plants (Aziz and Jassim 2018).

Hydrothermal synthesis of ZnO nanorods

Herein, for the synthesis of zinc oxide nanorods, we have used zinc nitrate as a precursor. In this experiment, we prepared an aqueous 0.2 M zinc nitrate solution. Then 100 mL of the zinc nitrate solution was taken in a beaker and kept on a magnetic stirrer, and 30 wt% ammonia solution was filled in the burette. At first, after the addition of a few mL of ammonia (NH$_3$) to the solution, there is the formation of a cloudy solution. After further addition of ammonia, the solution becomes colorless. The resultant reaction solution is transferred to an autoclave system and hydrothermally treated at 120 °C for 90 min. After the accomplishment of the reaction, the consequent system was allowed to cool down to room temperature. Then the synthesized powder was washed twice with DDW and ethanol, respectively, and kept for air drying at room temperature for 2 h. Finally, the ZnO nanorod was annealed for 2 h at 450 °C (Liu and Zeng 2003). Then the resultant product is ground into a fine powder using a mortar and pestle. Herein, when zinc nitrate is treated with ammonium hydroxide, the formation of zinc hydroxide takes place. This, upon hydrothermal treatment, gets converted into zinc oxide. The possible reaction mechanism may be as below.

$$Zn(NO_3)_2 + 2NH_4OH \rightarrow Zn(OH)_2 \xrightarrow{\Delta} ZnO.$$
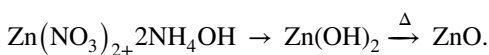
Preparation of nanocomposites

At the end of two different experimentation processes, we get Ag NPs and ZnO nanorods. Now we have to make composites of nanoparticles, i.e., nanocomposites of different concentrations. To make nanocomposites, we have followed solid state reaction pathways at room temperature.

For the preparation of the nanocomposite by the solid-state reaction at room temperature, we took ZnO nanorods and Ag NPs in the ratio of 95:05 weight ratios for 5% w/w and 90:10 weight ratio for 10% w/w. We put the sample in a mortar and ground it with a pestle for 3 h. It is very similar to the mechanical milling phenomena, i.e., by this, using the friction force, there is a cut down of bulk material into nanoregions. Using this method, we synthesized a uniform Ag–ZnO nanocomposite. During the reaction, we uniformly milled the nanomaterials in one direction. Practically, there is no formation of any primary bonds like ionic, covalent, or metallic bonding. However, between the NPs and nanorods, it looks like there are some weak attractive and repulsive physical forces are present. These forces are due to secondary bonds like Van Der wall's bond.

Characterization

Once a nanomaterial has been developed or synthesized, it becomes necessary to check its particle size, shape, surface charge, and morphology. As NPs are beyond the perception of human eyes, it becomes important to use various advanced characterization techniques. Spectroscopic and microscopic approaches are extensively used as characterization techniques. At the end of the experiment, we got fine white coloured ZnO nanorods and black coloured Ag NPs. Nanomaterial characteristics largely depend upon their size and form. The methods of characterization utilized are listed below.

A UV–Vis Spectrophotometer (Agilent Technologies, Cary 60) was used to examine the optical absorbance spectra of ZnO nanorods, Ag NPs, and nanocomposite of Ag–ZnO (5% w/w) and Ag–ZnO (10% w/w) in the wavelength range of 200–800 nm. X-ray diffraction spectra are used to describe the crystal structures of Ag NPs, ZnO nanorods, and Ag–ZnO nanocomposite (Bruker D8 advanced, Germany). Using a scanning electron microscope (Model JEOL-JSM-6360, Japan) and an acceleration voltage of 20 kV, the surface morphology of Ag NPs, ZnO nanorods, Ag–ZnO (10% w/w), and Ag–ZnO (5% w/w) nanocomposite were investigated. The FT-IR spectra were acquired using KBr pellets on an ALPHA Bruker FT-IR spectrometer. Wavenumbers ranging from 4000 to 400 cm^{-1} were used to characterize the samples. On a Nano ZS 90, the particle size and zeta potential were measured (Malvern, UK). Raman analysis using Ranishaw invia Raman spectroscope ranges from 0 to 3000 cm^{-1}.

Dye degradation assay

The catalytic activities of synthesized nanomaterials were studied against the Methylene Blue (MB) and Crystal Violet (CV) of aqueous dye solution for dye degradation. A reaction of degradation was carried out as follows: 0.08 g of nanomaterials (1 mg/mL) was thoroughly mixed with 80 mL of aqueous dye solution (10 mg/lit.) in a 100 mL beaker by continuous stirring for 24 h in the dark (For maximum Adsorption on the surface of our nanomaterial). After 24 h, the reaction solution was exposed to sunlight. The absorption intensity in a UV–Vis spectrophotometer at regular 15-min time intervals could be used to analyze the degradation of the aqueous dye solution. That leads to a colour change from blue/violet to colorless. The dye degradation percentage is obtained using Eq. (1),

$$\text{Dye Degradation (\%)} = 1 - \left(\frac{A_0}{A_t}\right) \times 100, \tag{1}$$

where, A_t represents the dye solution's absorbance intensity over time interval t, and A_0 is the dye solution's initial absorbance intensity.

Catalytic reduction reaction assay

The catalytic efficacy of synthesized Ag NPs was also investigated by reducing nitro-group-containing organic compounds in the presence of the strong reducing agent $NaBH_4$. While ZnO nanorods and their nanocomposite do not show strong catalytic reduction reactions against nitro-group containing compounds, the catalytic reduction reaction procedure was carried out as follows.

In a 3.0 mL eppendorf tube, 1.5 mL of 50 mM $NaBH_4$ ice cold solution was mixed with 1.5 mL of 1.0 mM nitro-group containing compounds aqueous solution and 200 µL of Ag NPs solution (1 mg/mL). The overall concentrations of nitro-group containing compounds and $NaBH_4$ were 1 and 50 mM, respectively. The solution was transferred to a standard quartz cell (path length of 1 cm and volume of 3.0 mL) for UV–Vis spectrophotometric analysis within the range from 200 to 800 nm. The absorption in a UV–Vis spectrophotometer at room temperature with a regular 30 s time interval could be used to analyze the reduction reaction(Baruah et al. 2013; Divband et al. 2013; Remita et al. 2013; Sahiner et al. 2013; Deka et al. 2014; Aditya et al. 2017).

Results and discussion

UV–Vis spectroscopic graph analysis

UV–Vis spectroscopy is a powerful tool for determining the formation and stability of metal NPs. Surface Plasmon Resonance (SPR) is responsible for the colour of colloidal Ag NPs, ZnO nanorods, and Ag–ZnO nanocomposites. SPR is caused by the collective oscillation of free-conduction electrons driven by an interacting electromagnetic field. The black-coloured Ag NPs sample powder, the white-pinkish coloured ZnO nanorod sample powder, and the grey coloured ZnO-Ag nanocomposites were all dissolved separately in deionized water and sonicated. The solution was then placed in a cuvette and subjected to UV–Vis light, with the absorbance of the solution being measured. For different nanoparticle solutions, the Surface Plasmon resonant (SPR) peak occurs at a distinct wavelength, and according to the theory of resonance, the maximum wavelength is absorbed at the resonant wavelength. According to the literature, typical Ag NPs exhibit the characteristic SPR at wavelengths ranging from 370 to 440 nm, with the wavelength varying with particle size (Zhao et al. 2006). Figure 1a displays colloidal SPR bands centering at 392 nm, confirming the existence of Ag NPs in the produced solution.

The UV–Vis spectra of Ag NPs, ZnO nanorods, and Ag–ZnO nanocomposites are shown in Fig. 1a–d. It has a well-defined absorption peak at 209 nm for Fig. 1d ZnO nanorods. For Ag–ZnO nanocomposite, i.e., Fig. 1b Ag–ZnO (10% w/w) nanocomposite and Fig. 1c Ag–ZnO (5% w/w) nanocomposite, have the maximum absorption peak both at 209 and 392 nm, respectively.

XRD study

The formation of poly-dispersed crystalline nano-material is revealed by the XRD pattern. Figure 2a–d shows the XRD patterns of synthesised Ag NPs, ZnO, and their nanocomposites. The peak position describes the translational symmetry of the unit cell, essentially its size and structure.
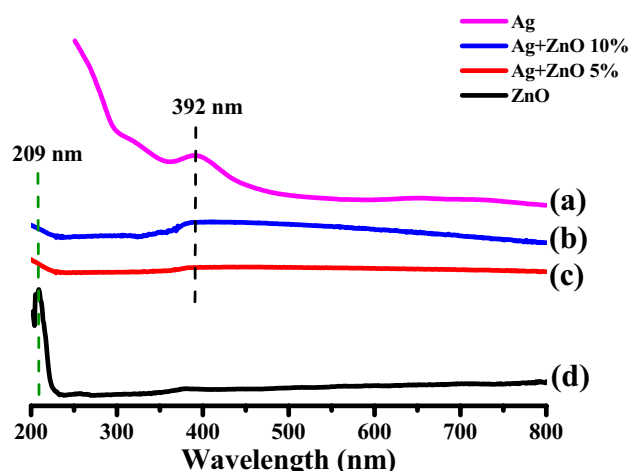

Fig. 1 UV–Vis Spectra of (*a*) Ag NPs (*b*) Ag–ZnO (10% w/w) nanocomposite (*c*) Ag–ZnO (5% w/w) nanocomposite (*d*) ZnO nanorods

Figure 2a shows the XRD pattern of Ag NPs. Bragg's reflections can be observed in the XRD pattern 2θ at 38.12, 44.31, 64.46, and 77.41, which correspond to the (111), (200), (220), and (311) planes, respectively, indicating that Ag NPs were nanocrystals with face centered cubic (FCC) structure. The patterns were consistent and matched with card No. 01-089-3722 in the Joint Committee on Powder Diffraction Standards (JCPDS) database.

The ZnO nanorods (Fig. 2d) are polycrystalline with a hexagonal wurzite-type structure (JCPDS card No. 01-076-0704). The ZnO nanorods were observed at 2θ values at 31.737, 34.379, 36.215, 47.484, 56.536, 62.777, 66.304, 67.868, 69.009, 72.465, 76.867 and 81.270 representing (h k l) values (100), (002), (101), (102), (110), (103), (200), (112), (201), (004), (202) and (104) planes, respectively (Liu and Zeng 2003; Polsongkram et al. 2008; Upadhaya and Dhar Purkayastha 2020). Both JCPDS cards give confirmation of the purity of synthesized nanomaterial and nanocomposite (Fig. 2b, c). No further impurities are present in the synthesized samples.

The Debye–Scherer's formula (Eq. (2)) was used to calculate the crystallite size of the nanomaterials from the Full Width at Half Maxima (FWHM) denoted by β and the Diffraction angle (θ),

$$D = \frac{0.9\lambda}{\beta \cos \theta}, \tag{2}$$

where λ is the wavelngth of X-ray used for diffraction (0.15406 nm).

The crystallite size for various samples is calculated using the above formala and is represented in Table 1 for Ag NPs and in Table 2 for zinc oxide nanorods (Suryavanshi et al. 2018a).

Morphology Index (MI)

The interrelation between particle size and morphology determines the specific surface area of a nanoparticle. FWHM is used to determine MI. MI is calculated using the following formula:

$$MI = \frac{FWHM_h}{FWHM_h + FWHM_p}. \tag{3}$$

The particulate FWHM value of a peak is $FWHM_p$, and the highest FWHM value obtained from peaks is $FWHM_h$.

MI value of Ag NPs varies from 0.5 to 0.8797 (Table 1) and ZnO nanorods calculated values vary from 0.5 to 0.8682 (Table 2). It is correlated with the crystalline particle size and Specific Surface Area (SSA). SSA value of Ag NPs is 6.4183–38.7495 m^2/g (Table 1) and nanorods show SSA value from 6.9981 to 40.5954 m^2/g (Table 2). According to the estimated data, MI is linearly proportional to particle size and inversely proportional to SSA with a slight variation. Figures 3a, b and 4a, b show the results. The deviations and correlations between the figures are indicated by the linear fit (Vinila et al. 2014; Suryavanshi et al. 2018b).

Surface morphology

The SEM image from Fig. 5a–d reveals the formation of a cluster of spherical beads, similar to the structure of Ag NPs, with a non-uniform distribution. Figure 5a indicates the formation of relatively spherical-shaped Ag NPs with
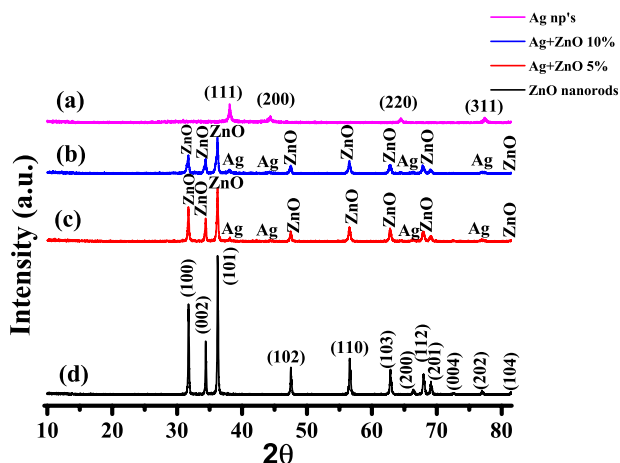
Fig. 2 XRD Pattern of (*a*) Ag NPs (*b*) Ag–ZnO (10% w/w) nanocomposite (*c*) Ag–ZnO (5% w/w) nanocomposite (*d*) ZnO nanorods

Table 1 XRD analysis and calculation of various parameters for Ag NPs

Sr. No.	Peak position: 2θ (degree)	Full width half maxima (degree)	Full width half maxima (radians)	Particle size D (nm)	d-spacing (Å)	For Ag unit cell edges: $a = b = c$ (Å)	Specific surface area (m^2/g)	Morphological indexing
1	38.0649	0.0945	0.001649	88.95	2.36409	4.0855	6.4183	0.8797
2	44.3883	0.3779	0.006595	22.71	2.04088		25.14202	0.64652
3	64.4939	0.3779	0.006595	24.86	1.44487		22.96538	0.64652
4	77.4587	0.6912	0.012064	14.73	1.23121		38.7495	0.5

Table 2 XRD analysis and calculation of various parameters for ZnO nanorods

Sr. No.	Peak position:2θ (degree)	Full width half maxima (degree)	Full width half maxima (radians)	Particle size D (nm)	d-spacing (Å)	For Ag unit cell edges: $a = b \neq c$ (Å)	Specific surface area (m²/g)	Morphological indexing
1	31.77	0.0827	0.00144	100.11	2.81665	($a = b$ 3.2530)	10.589	0.8207
2	34.3903	0.059	0.00103	140.91	2.6078	($c = 5.2130$)	7.5228	0.8648
3	36.2294	0.059	0.00103	141.63	2.47953		7.4844	0.8648
4	47.4952	0.0576	0.001	151.48	1.9128		6.9981	0.8682
5	56.5702	0.1181	0.00206	76.43	1.62693		13.8691	0.7618
6	62.834	0.0945	0.00165	98.47	1.47898		10.7656	0.7997
7	66.3078	0.1417	0.00247	67.05	1.40968		15.8099	0.7274
8	67.9139	0.1417	0.00247	67.68	1.3802		15.6637	0.7274
9	69.0977	0.0945	0.00165	102.03	1.35942		10.3902	0.7997
10	72.6377	0.3779	0.00659	26.11	1.30165		40.5954	0.5
11	76.925	0.1728	0.00301	58.83	1.23842		18.0192	0.6864

Fig. 3 Morphological index vs particle size of (**a**) Ag NPs (**b**) ZnO nanorods
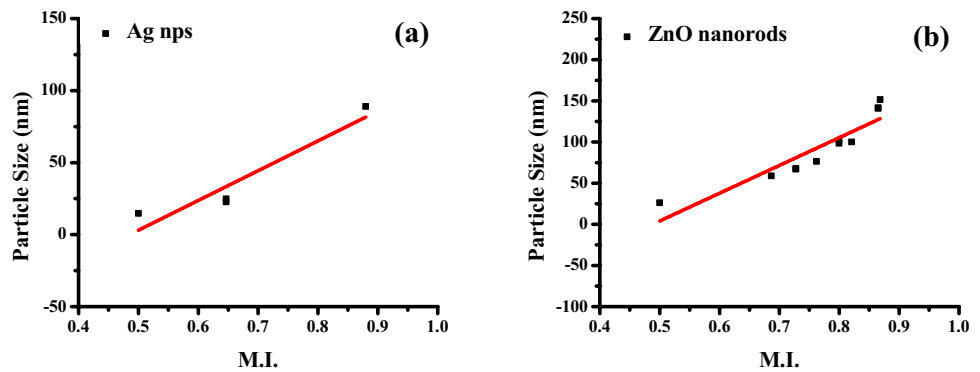
Fig. 4 Morphological index vs specific surface area of (**a**) Ag NPs (**b**) ZnO nanorods
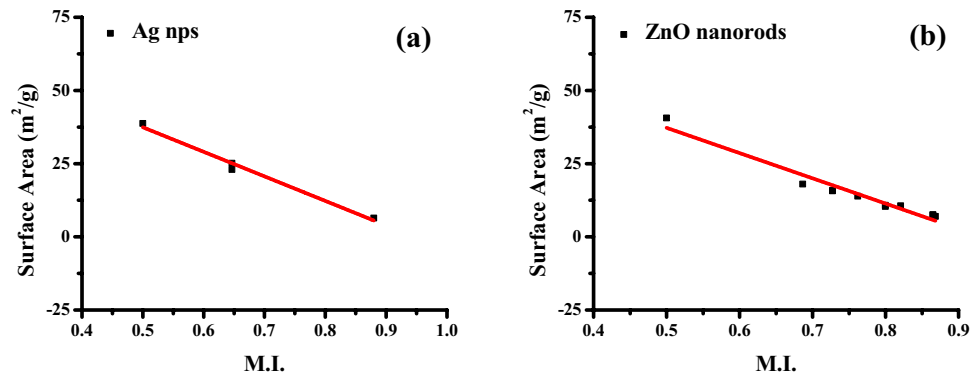
an average diameter of 400 nm. The size of particles was increased due to agglomeration. The formation of homogeneously distributed nanocomposite of the Ag NPs is shown in Fig. 5b, Ag–ZnO (10% w/w), and Fig. 5c, Ag–ZnO (5% w/w). The SEM images reveal a random distribution of nanomaterials with large diameter nanorods of zinc oxide NPs and spherical-shaped Ag NPs. We clearly observe in the images that the nanorod gets broken as a result of 3 h of mechanical grinding. Figure 5d ZnO nanorods demonstrate

the production of hexagonal nanorods with lengths of several thousand nm. It indicates the formation of a controlled size and regular hexagonal shape of the nanorods. The nanorods have solid hexagonal planes projecting out of the crystal seed layer, and their width is in the range of in between 100 and 1000 nm (Huang et al. 2015).

FE-SEM i.e. field emission scanning electron microscopy, analyze the size and morphology of sample. Figure 5e–h illustrates the FE-SEM analysis of Ag np's, ZnO nanorods
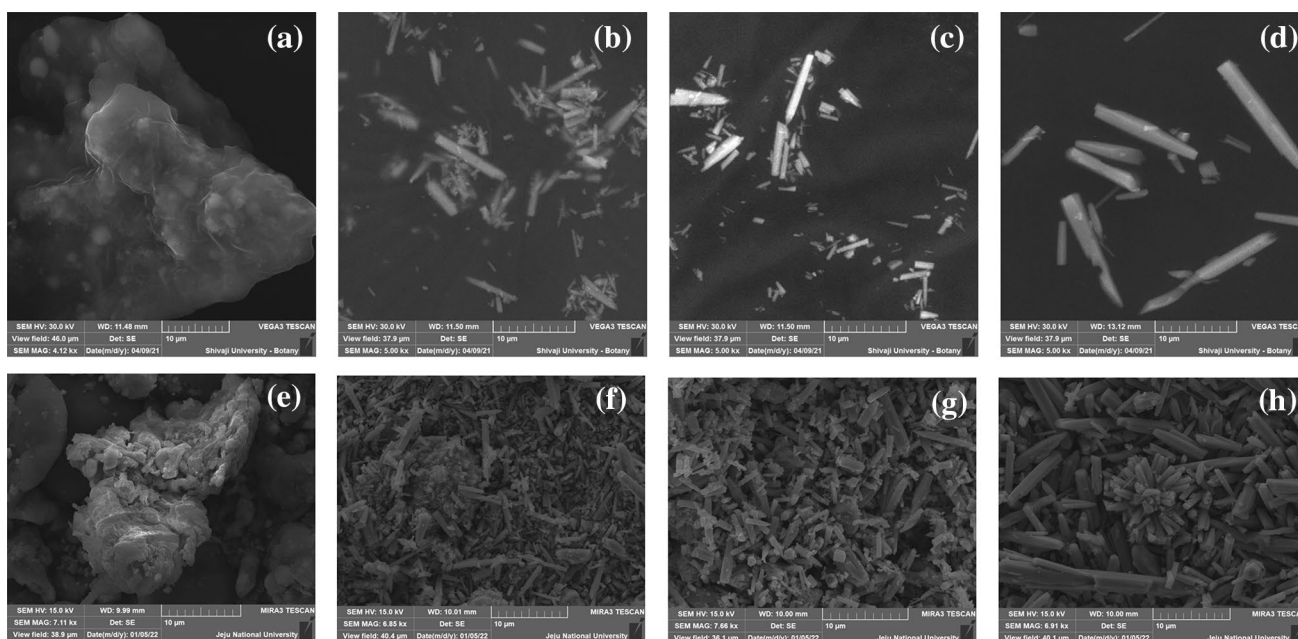
Fig. 5 SEM analysis of (**a**) Ag np's (**b**) Ag–ZnO (10% w/w) nanocomposite (**c**) Ag–ZnO (5% w/w) nanocomposite (**d**) ZnO nanorods and FESEM analysis of (**e**) Ag np's (**f**) Ag–ZnO (10% w/w) nanocomposite (**g**) Ag–ZnO (5% w/w) nanocomposite (**h**) ZnO nanorods

and their composites. However, looking at the Fig. 5e i.e. FE-SEM image of Ag np's reveals the smaller spherical NPs and some larger particles were found infrequently agglomerated together (Twu et al. 2008). Figure 5f, g and include the FE-SEM image of Ag–ZnO (10% w/w) and Ag–ZnO (5% w/w). Nevertheless, it is pretty clear that Ag np's are randomly dispersed around the ZnO nanorods, in which it is seen that the number of Ag np's is greater in the Ag–ZnO (10% w/w) as compared to the Ag–ZnO (5% w/w) (Wu et al. 2013). Furthermore, FE-SEM image of ZnO sample is shown in Fig. 5h. It can be clearly seen that the ZnO sample comprises needle-like nanorods, addition to that, ZnO nanorods also show the unvarying uniform growth in aligned direction and a mean diameter of about 4000–7000 nm (Gao et al. 2013).

FT-IR analysis

FT-IR is the fingerprint for atomic and molecular vibrations. Here, we observe different types of vibrations of the analyzed samples. The bending vibration of –OH groups was linked to the transmittance band at 1555 cm^{-1} for Fig. 6a Ag NPs. The band at 1361 cm^{-1} is attributed to the –CH$_2$ group's deformation stretching. The bending of the C–C bond is described by the peak at 515 cm^{-1}. The band at 3424 cm^{-1} was attributed to the hydrogen bond stretching vibration of –OH groups in the Fig. 6b Ag–ZnO (10% w/w) nanocomposite, Fig. 6c Ag–ZnO (5% w/w) nanocomposite, and Fig. 6d ZnO nanorods. The stretching vibration of
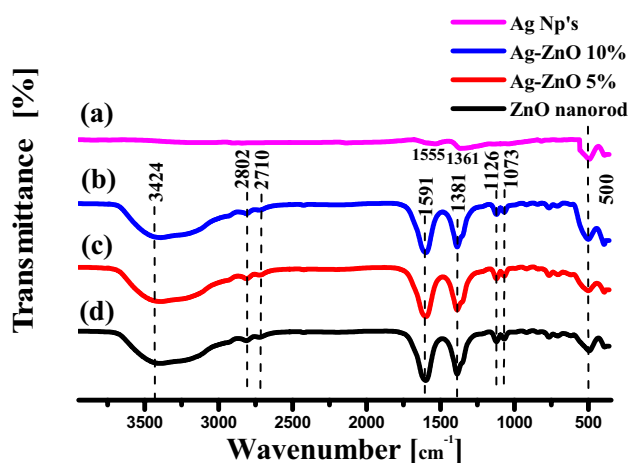

Fig. 6 FTIR spectra of (*a*) Ag NPs (*b*) Ag–ZnO (10% w/w) nanocomposite (*c*) Ag–ZnO (5% w/w) nanocomposite (*d*) ZnO nanorods

–CH was attributed to the transmittance band at 2802 cm^{-1} (Paulkumar et al. 2017; Zhang et al. 2019). The transmittance bands of the asymmetric stretching vibration –CH$_3$ and –CH$_2$ groups were observed at 2802 and 2710 cm^{-1}, respectively, while the peaks of the N–H (amide II) and vC-N (amide III) groups were observed at 1591 and 1381 cm^{-1}. The stretching vibrations of C–O stretching cause the band to appear at 1126 and 1073 cm^{-1} (Abutalib and Rajeh 2020). The stretching vibrations of C–O were blamed for the band

at 1073 cm^{-1}. The transmittance peak at 486 cm^{-1} is also attributed to Zn–O vibration (Beura et al. 2021).

Raman spectroscopic analysis

The Raman spectra of Ag NPs and Ag–ZnO (10% w/w) and Ag–ZnO (5% w/w) nanocomposites are exhibited in Fig. 7a, b, and c, respectively. The characteristic D and G bands for Ag NPs and Ag–ZnO (10% w/w) and Ag–ZnO (5% w/w) nanocomposites were observed at 1366, 1386, and 1373 cm^{-1} for D bands and 1586, 1588, and 1586 cm^{-1} for G bands, respectively. However, the I_D/I_G ratios of Ag NPs and Ag–ZnO (10% w/w) and Ag–ZnO (5% w/w) nanocomposites were 0.83, 0.86, and 0.93, respectively(Sang et al. 2017; Hedberg et al. 2021).

The optical phonons of ZnO have modes A1 + 2B1 + E1 + 2E2 which reveal a wurtzite structure from the C6v symmetry group. The polar phonons E1 and A1 split into longitudinal (LO) and transverse (TO) optical phonons. In Raman spectra, the B1 mode is not present. On the other hand, Nonpolar modes (E2) are Raman active and have two frequencies: E2 (high) and E2 (low), which correspond to the vibrations of the oxygen and Zn atoms, respectively.

The obtained peaks (Fig. 7a) are in good agreement with the ZnO phase. ZnO has a Raman shift of 419 cm^{-1}, which corresponds to the E2 high-frequency mode. The peak at 593 cm^{-1}, displayed in E1 (LO) mode, shows the structural flaws in ZnO. The peak in ZnO nanorods around 1145 cm^{-1} is owing to multiple-phonon scattering; thus, the intensity of these peaks in Ag–ZnO (10% w/w) and Ag–ZnO (5%) nanocomposites is lower (Chanda et al. 2017; Meti et al. 2018).

Particle size distribution

Dynamic light scattering is used to determine the hydrodynamic diameter of produced NPs, nanorods, and nanocomposites. Figure 8 shows the DLS (dynamic light scattering),

which reveals the hydrodynamic diameter of the synthesized NPs. When light passes through a colloidal solution, it bombards microscopic particles and scatters them in every possible direction (i.e., Rayleigh scattering). Even if the incident light is monochromatic or non-divergent, like a laser, we see a fluctuation in the intensity of light. The fluctuation in light intensity is caused by Brownian motion in solution, which always occurs. The dimension of a particle can be determined as a result of the Brownian motion of the particle. Dynamic light scattering, also known as photon correlation scattering, is a common name for this approach.

DLS analysis reveals the average size of Ag NPs (Fig. 8a) to be 340.8 nm. The sharp peak of Ag NPs indicates mono-dispersed type of synthesized NPs. Figure 8d shows the distribution of ZnO nanorods in the size range of 2000–4400 nm. The average particle size of ZnO nanorods is 3062 nm. Broad size distributions of ZnO nanorods show
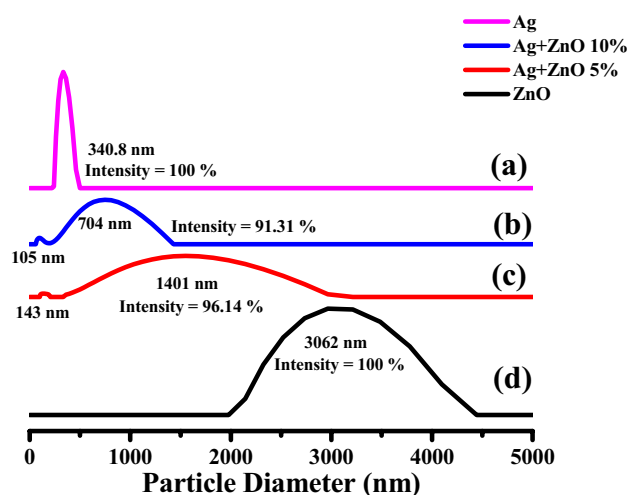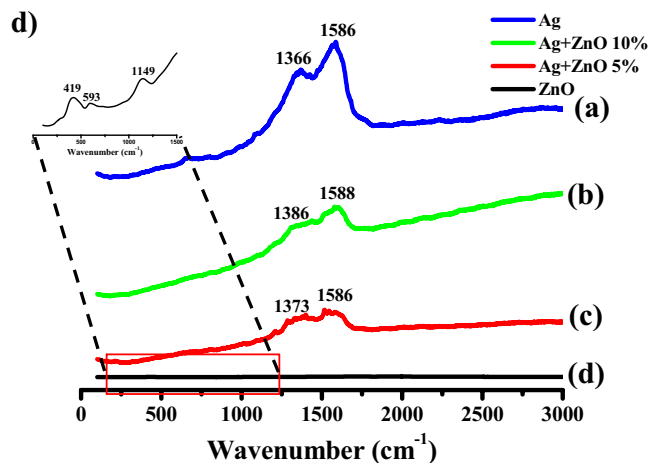
Fig. 8 DLS particle size distribution of (*a*) Ag NPs (*b*) Ag–ZnO (10% w/w) nanocomposite (*c*) Ag–ZnO (5% w/w) nanocomposite (*d*) ZnO nanorods

Fig. 7 Raman spectra of (*a*) Ag NPs (*b*) Ag–ZnO (10% w/w) nanocomposite (*c*) Ag–ZnO (5% w/w) nanocomposite (*d*) ZnO nanorods

their poly-dispersed nature. Figure 8b, c depict the particle size distribution of nanocomposites. As compared to ZnO nanorods, the particle size of both nanocomposites is reduced due to milling. The particle size of the Ag–ZnO (10% w/w) nanocomposite (Fig. 8b) is 105–704 nm. While the Ag–ZnO (5% w/w) nanocomposite (Fig. 8c) is 143 and 1401 nm. Both nanocomposites are poly-disperse in nature (Mukherjee et al. 2014).

Zeta potential

The zeta potential in Fig. 9a–d indicates the stability of the NPs produced. The sample's Zeta potential reveals the colloidal solution's dispersion stability. It also demonstrates the NPs mobility. The zeta potential's higher positive or negative value indicates stability.

The zeta potential of Ag NPs (Fig. 9a) demonstrates that they have low stability, namely −9.3 mV. The emergence of negative charge on the surface of Ag NPs might be analyzed. The negative charge on ZnO nanorods (Fig. 9d) is −30.5 mV. Due to negative–negative repulsion, the high negative zeta potential (ξ) value supports the long-term stability, good colloidal nature, and high dispersion of ZnO nanorods. −34.6 mV is the value of the Ag–ZnO (10% w/w) nanocomposite (Fig. 9b). −30.5 mV for Ag–ZnO (5% w/w) nanocomposite (Fig. 9c). Figure 9a–d shows the zeta potential of the nanoparticle and nanocomposite acquired through analysis. A steadier dispersion is predicted by higher zeta potentials. A value of 40–60 mV suggests excellent nanoparticle stability in most cases (Jyoti et al. 2016; Nagar and Devra 2019).
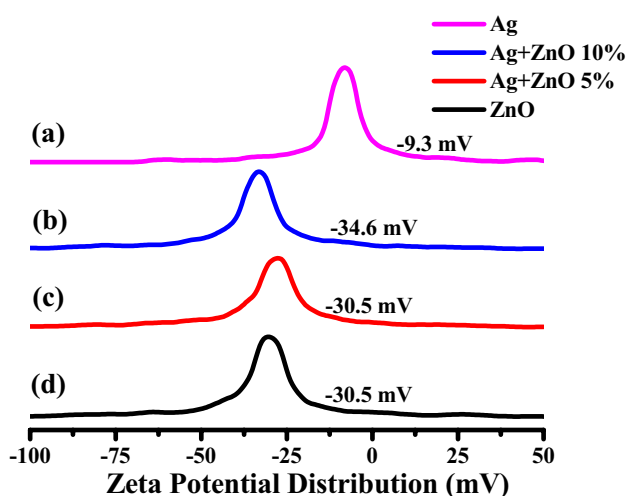

Fig. 9 Zeta potential Distribution of (*a*) Ag NPs (*b*) Ag–ZnO (10% w/w) nanocomposite (*c*) Ag–ZnO (5% w/w) nanocomposite (*d*) ZnO nanorods

Dye degradation

The photocatalytic activity of Ag NPs, ZnO nanorods and their nanocomposites were studied by mixing them into MB and CV aqueous dye solution for degradation in the presence of the sunlight. As the reaction proceeds, the dye solution gets decolorized. Among all irradiation techniques sunlight gives faster decolorizing results in the presence of Nanocatalyst and it's easy to commercialize (Liu et al. 2019a).

Degradation of methylene blue (MB) dye

The absorbance spectrum of MB gives a peak at 663 nm. We studied the photocatalytic activity of all synthesized nanomaterials and their composites for MB, in which Ag NPs shown 83% degradation in 180 min. The percentage degradation of MB dye solution in presence of Ag NPs is shown in Fig. 10c. When Ag–ZnO nanocomposite was used as a catalyst, it shows different activity Ag–ZnO (10% w/w) nanocomposite and Ag–ZnO (5% w/w) nanocomposite shows 82% and Ag–ZnO (5% w/w) 91% of the degradation respectively. Ag–ZnO (10% w/w) nanocomposite takes 165 min for degradation, and after 120 min, the maximum absorbance value is nearly same. In the case of Ag–ZnO (5% w/w) nanocomposite the absorbance intensity from 150 to 195 min is almost similar. Figures 11c and 12c show the degradation percentages of Ag–ZnO (10% w/w) nanocomposite and Ag–ZnO (5% w/w) nanocomposite. ZnO photocatalyst involve 195 min to degrade 96.37% of dye and Fig. 12c indicates the result of dye degradation (%). The plot of $\ln(A_0/A_t)$ versus time (min) gives a straight line passing through the origin with a positive slope value, and it is known as the rate constant (*k*). The *k* value of Ag NPs is 0.00925 min^{-1}, as shown in Fig. 10b. The *k* values for Ag–ZnO (10% w/w) nanocomposite and Ag–ZnO (5% w/w) nanocomposite are 0.01242 and 0.01276 min^{-1} respectively and these values are taken from Figs. 11b and 12b. From Fig. 13b, the calculated *k* value of ZnO nanorods is 0.01701 min^{-1} (Joseph and Mathew 2015).

Degradation of crystal violet (CV) dye

CV is generally used in biology to classify bacteria (Grams Method). This is also used as an effective medicine in poultry. It is the primary toxic organic dye used in the textile industry. Pure CV solution shows the absorbance peak at 583 nm. As shown in Fig. 14c, the degradation of CV in presence of Ag NPs took place in 120 min for 97% of the degradation, however 70% of the degradation of organic dye occurred in the first 90 min. The results for Ag–ZnO (10% w/w) nanocomposite and Ag–ZnO (5% w/w) nanocomposite are identical. As shown in Figs. 15c and 16c, they both degrade 50% of the dye in 0–15 min and the remaining 83%
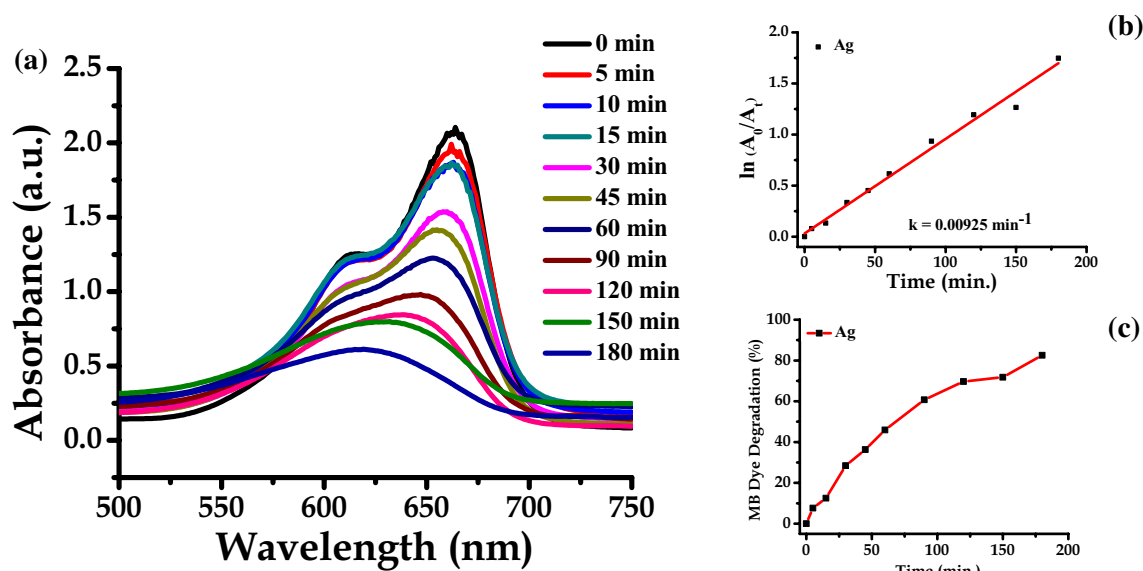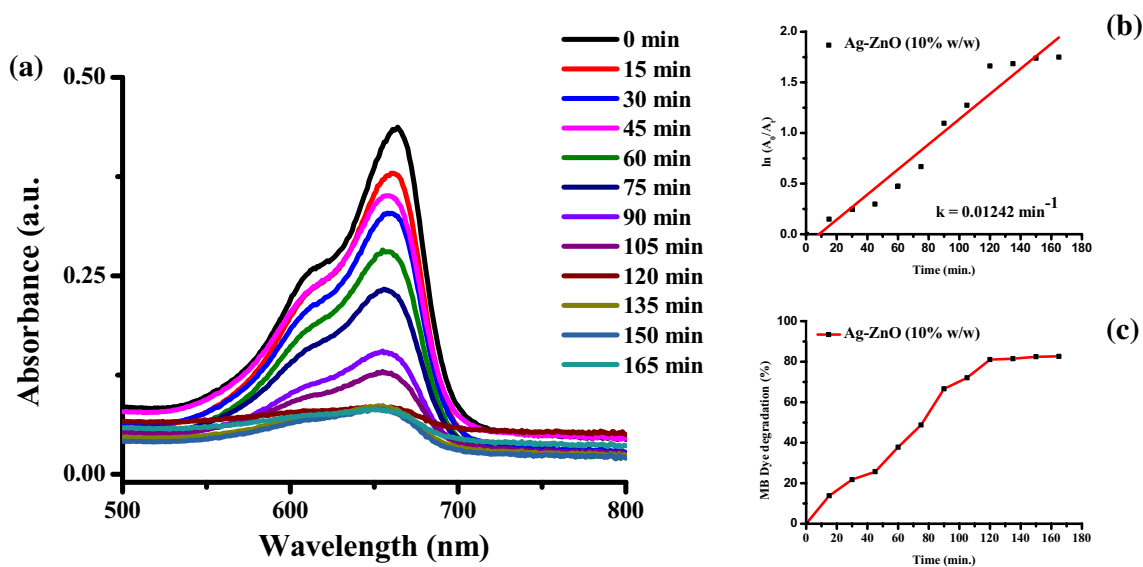
Fig. 10 Absorption spectra of reduction of methylene blue dye (**a**), Kinetics of catalytic reduction (**b**) and % degradation of methylene blue dye (**c**) in the presence of catalyst Ag NPs

Fig. 11 Absorption spectra of reduction of methylene blue dye (**a**), Kinetics of catalytic reduction (**b**) and % degradation of methylene blue dye (**c**) in the presence of catalyst Ag–ZnO (10% w/w) nanocomposite

in 105 min. The ZnO nanorods degrade by 89% in 275 min in the presence of UV light, as shown in Fig. 17c. After Ag NPs, Ag–ZnO (10% w/w) nanocomposite, Ag–ZnO (5% w/w) nanocomposite and ZnO nanorods are used as the photocatalyst, The k value of nanomaterials are 0.02810, 0.0144, 0.01444, and 0.00688 min^{-1} respectively, and all are calculated from Figs. 14b, 15b, 16b and 17b, respectively(Liu et al. 2019b). Each dye reacts against synthesized

nanomaterials and observed value of dye degradation (%) and rate constant of reaction are represented in Table 3.

Possible mechanistic pathway of photocatalysis

When sunlight is irradiated on a photocatalyst with photonic energy (hν) greater than or equal to bandgap energy (E_g), electron–hole pairs (EHP) are generated. The electron is located in the conduction band (CB) which is excited from
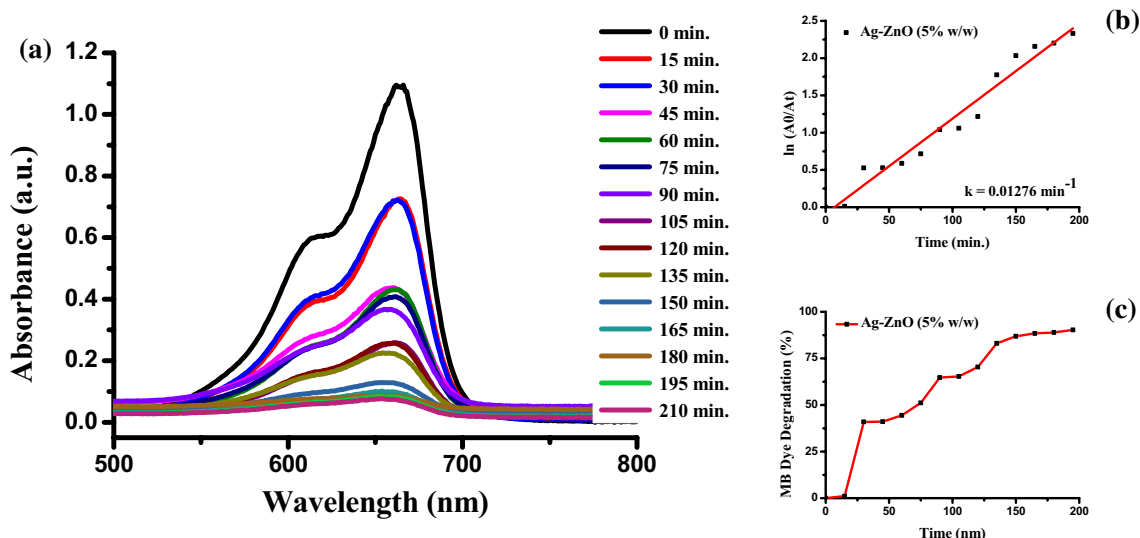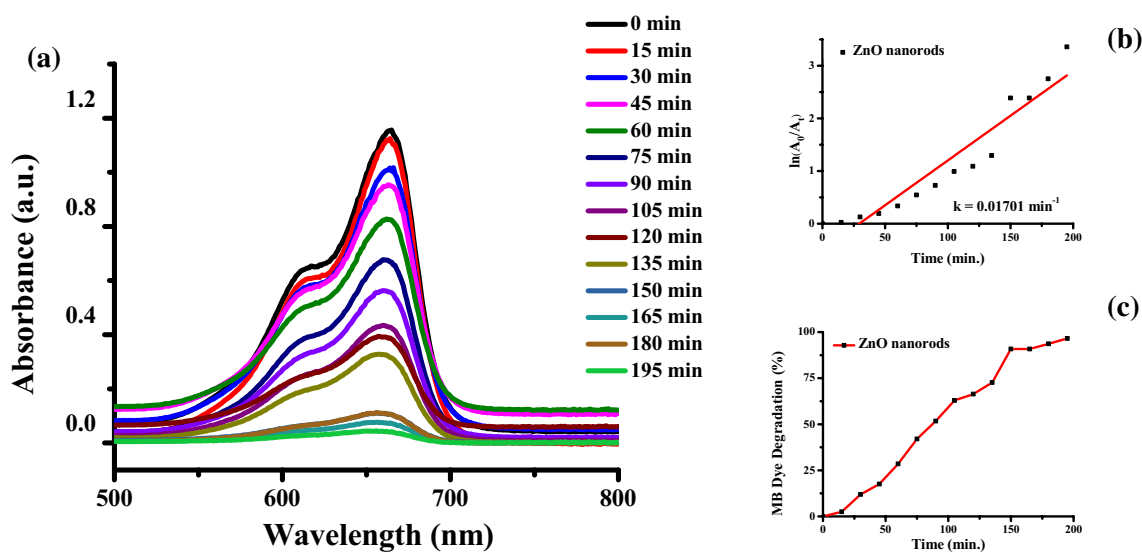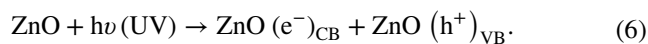
Fig. 12 Absorption spectra of reduction of methylene blue dye (**a**), Kinetics of catalytic reduction (**b**) and % degradation of methylene blue dye (**c**) in the presence of catalyst Ag–ZnO (5% w/w) nanocomposite
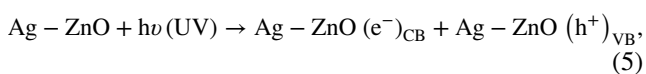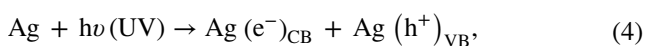

Fig. 13 Absorption spectra of reduction of methylene blue dye (**a**), Kinetics of catalytic reduction (**b**) and % degradation of methylene blue dye (**c**) in the presence of catalyst ZnO nanorods

the valence band (VB) and thus in the VB there is lacuna of e^- i.e. the hole (h^+) makes its appearance as shown in Eqs. (4)–(6).

$$Ag + h\upsilon\,(UV) \rightarrow Ag\,(e^-)_{CB} + Ag\,(h^+)_{VB}, \tag{4}$$

$$Ag - ZnO + h\upsilon\,(UV) \rightarrow Ag - ZnO\,(e^-)_{CB} + Ag - ZnO\,(h^+)_{VB}, \tag{5}$$

$$ZnO + h\upsilon\,(UV) \rightarrow ZnO\,(e^-)_{CB} + ZnO\,(h^+)_{VB}. \tag{6}$$

The e^- and h^+ scavengers trap the EHP to prevent recombination. h^+ is acted as a strong oxidizing species. The e^- and h^+ are reacting with chemical species like O_2, $\cdot OH^-$ and water, resulting in the formation of strong oxidizing species like hydrogen peroxide (H_2O_2), superoxide radical anion ($\cdot O_2^-$) and hydroxyl radical ($\cdot OH$) as shown in Eqs. (7)–(10).
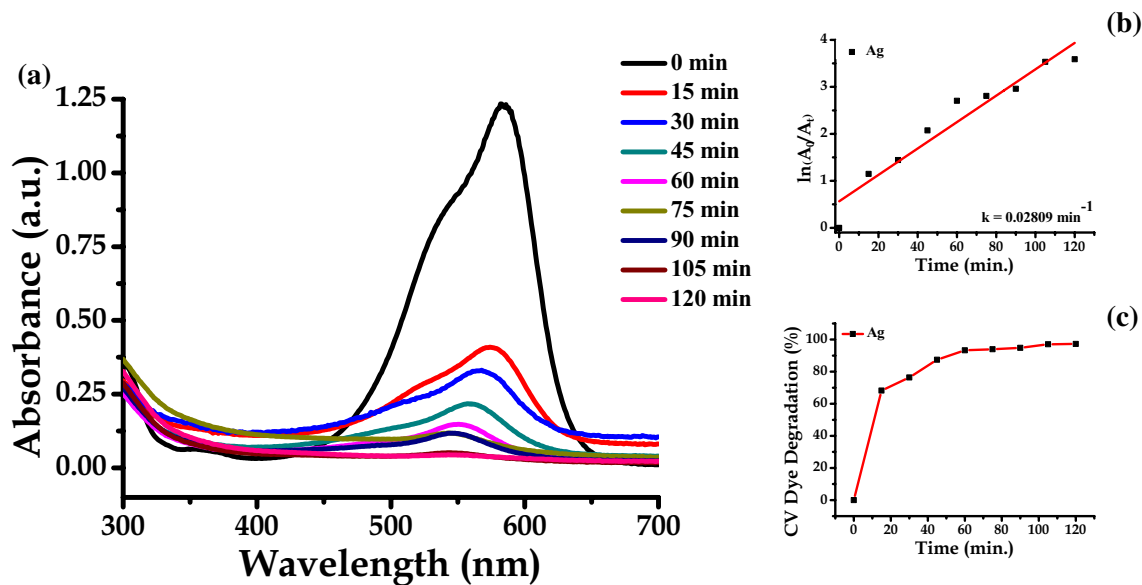
Fig. 14 Absorption spectra of reduction of crystal violet dye (**a**), Kinetics of catalytic reduction (**b**) and % degradation of methylene blue dye (**c**) in the presence of catalyst Ag NPs
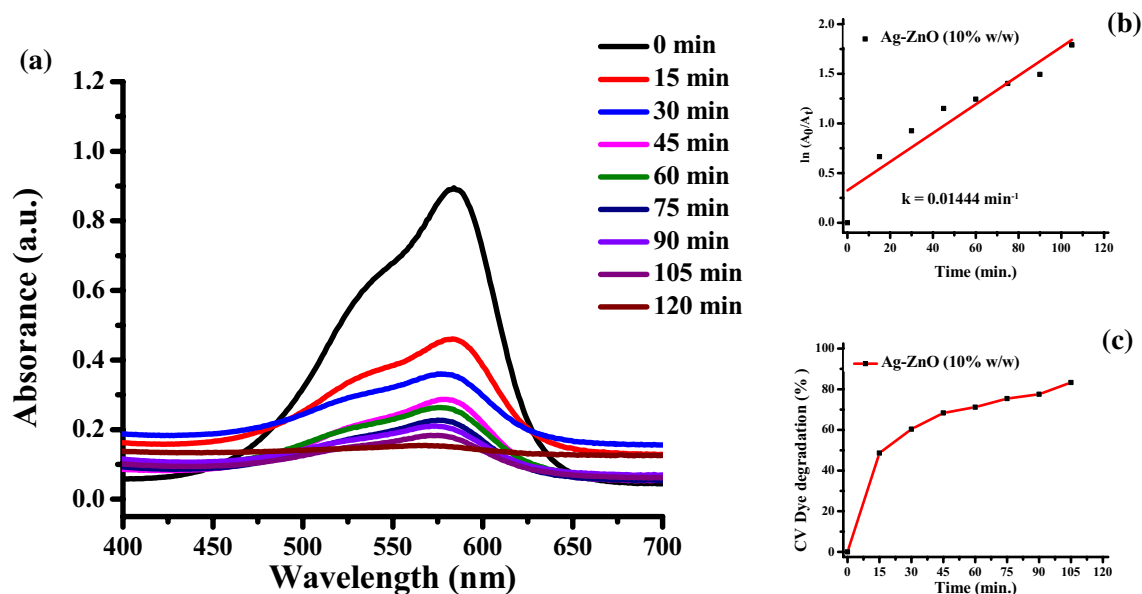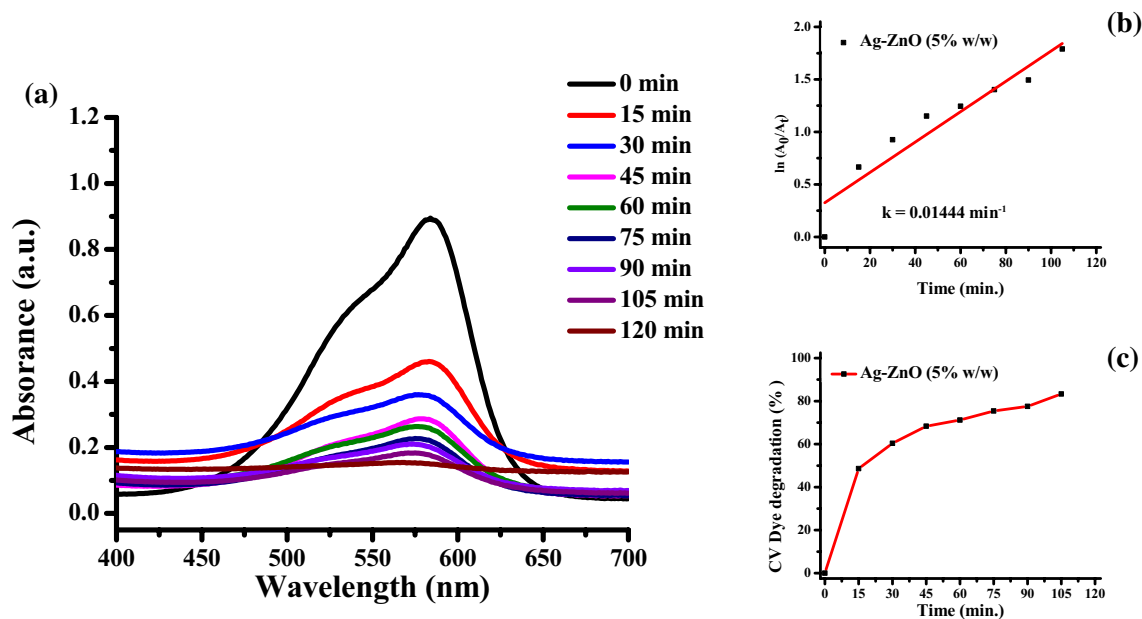

Fig. 15 Absorption spectra of reduction of crystal violet dye (**a**), Kinetics of catalytic reduction (**b**) and % degradation of methylene blue dye (**c**) in the presence of catalyst Ag–ZnO (10% w/w) nanocomposite

$$e^- + O_2 \rightarrow {}^{\cdot}O_2. \tag{7}$$

Reaction of h^+ with OH^- and H_2O,

$$h^+ + OH^- \rightarrow {}^{\cdot}OH, \tag{8}$$

$$h^+ + H_2O \rightarrow {}^{\cdot}OH + H^+. \tag{9}$$

Furthermore, oxidizing species reaction are given below,

$${}^{\cdot}O_2^- + H^+ \rightarrow {}^{\cdot}HO_2, \tag{10}$$

$$2{}^{\cdot}HO_2 \rightarrow H_2O_2 + O_2, \tag{11}$$

$$H_2O_2 + e^- \rightarrow OH^- + {}^{\cdot}OH, \tag{12}$$

Fig. 16 Absorption spectra of reduction of crystal violet dye (**a**), Kinetics of catalytic reduction (**b**) and % degradation of methylene blue dye (**c**) in the presence of catalyst Ag–ZnO (5% w/w) nanocomposite
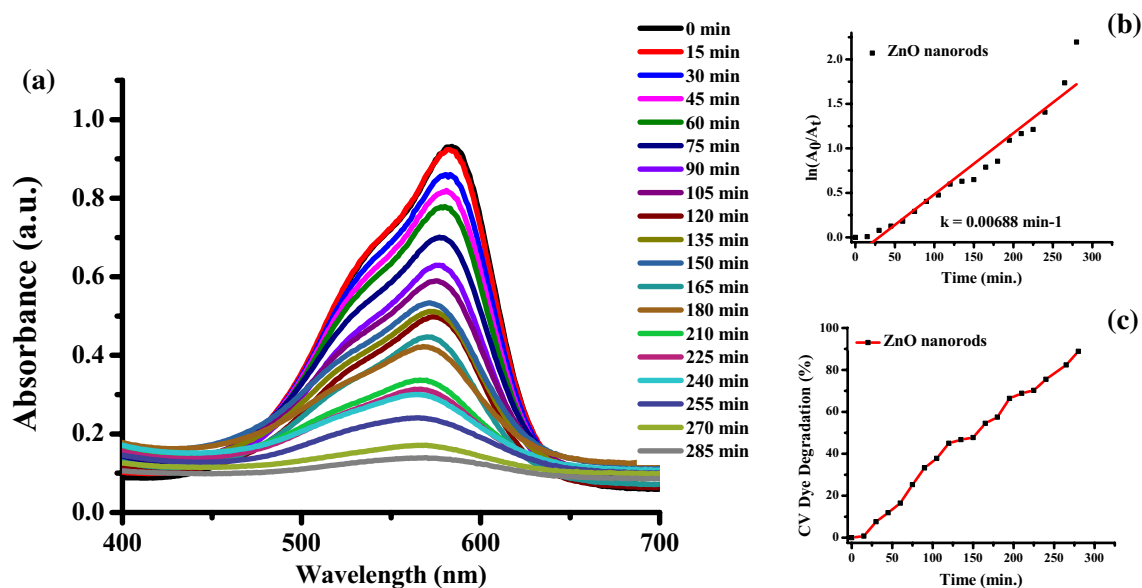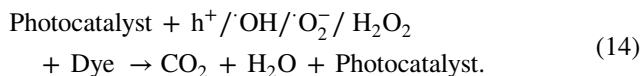

Fig. 17 Absorption spectra of reduction of crystal violet dye (**a**), Kinetics of catalytic reduction (**b**) and % degradation of crystal violet dye (**c**) in the presence of catalyst ZnO nanorods

Table 3 Percentage of dye degradation and rate constants of synthesized nanomaterials

Nanomaterials	Methylene blue dye		Crystal violet dye	
	% Dye degradation	Rate constant (k) (min^{-1})	% Dye degradation	Rate constant (k) (min^{-1})
Ag NPs	83	0.00925	97	0.02810
Ag–ZnO (10% w/w) nanocomposite	82.67	0.01242	83	0.0144
Ag–ZnO (5% w/w) nanocomposite	91	0.01276	83	0.01444
ZnO nanorods	96.37	0.01701	89	0.00688

$$H_2O_2 + \cdot O_2 \rightarrow OH^- + \cdot OH + O_2. \tag{13}$$
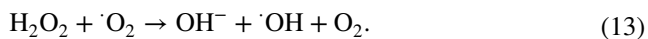
The organic pollutant gets adsorbed and reacted on the surface of the photocatalyst. The resulting superoxide radical anion ($\cdot O_2^-$), Hydroxyl radical ($\cdot OH$) and hydrogen peroxide (H_2O_2) formation, which are dominant oxidizing species. This oxidizing species attacks on the surface of the photocatalyst, where the pollutant is adsorbed. The pathway of photocatalytic reaction is the oxidation of organic pollutants (as mentioned above) and converting them to green compounds like CO_2 and H_2O as shown in Eq. (14).

$$\begin{aligned} \text{Photocatalyst} + \text{h}^+ / \cdot OH / \cdot O_2^- / H_2O_2 \\ + \text{Dye} \rightarrow CO_2 + H_2O + \text{Photocatalyst}. \end{aligned} \tag{14}$$

The mechanistic pathway of dye degradation is represented in Fig. 18.

Among the synthesized samples, the ZnO nanorods exhibit excellent photocatalytic activity and decolorize the MB dye. Ag NPs are highly efficient and were observed to be very active in the degradation of CV dye. Thus, the photocatalyst could be used to degrade pollutants in water, especially for the treatment of textile effluents (Marimuthu et al. 2020).

Ag NPs as nano-catalyst

A nano-catalyst is a non-directly involved foreign material added to a chemical system. These days, describing a Nano-catalyst might be as simple as starting with NPs. When a Nano-catalyst is used in organic transformation reactions, the reaction rate (k) can be increased, and

reactions can also take place at room temperature. In the chemical manufacturing industry, the reduction process is critical and vital to organic transformation. Nitro-group containing aromatic chemicals are of paramount importance due to their high significance in heterocyclic aromatic compound synthesis, pharmaceutical compound synthesis, agro-chemical synthesis, and so on. In the many earlier reported papers (Baruah et al. 2013; Deka et al. 2014; Aditya et al. 2017; Liang et al. 2018; Guo et al. 2019) the conversion of 4-nitrophenol to 4-aminophenol by the catalytic reduction reaction is carried out in the presence of metallic NPs. So, the reduction reaction is not carried out without a suitable catalyst (Kuroda et al. 2009). Hydrothermally synthesized ZnO nanorods and their nanocomposites are not ideal for catalytic reduction reactions with a nominal rate constant. However, the chemically synthesis of metallic NPs is expensive and also, releases toxic byproducts. We investigated numerous chemical transformation processes employing biologically synthesized Ag NPs in the current reaction. This research work reports excellent catalytic activity for Nitro-group containing aromatic chemicals. The development of the reaction is monitored using a UV–Vis spectrophotometer.

Reduction of 4-Nitrophenol

The freshly prepared 4-nitrophenol (4-NP) solution is a pale-yellowish coloured that changes to bright yellow with a strong absorbance peak at 400 nm to form nitrophenolate ion due to the addition of $NaBH_4$ solution (Zhang et al. 2011; Chiou et al. 2013). As the reaction progresses, the functional Nitro ($-NO_2$) group is
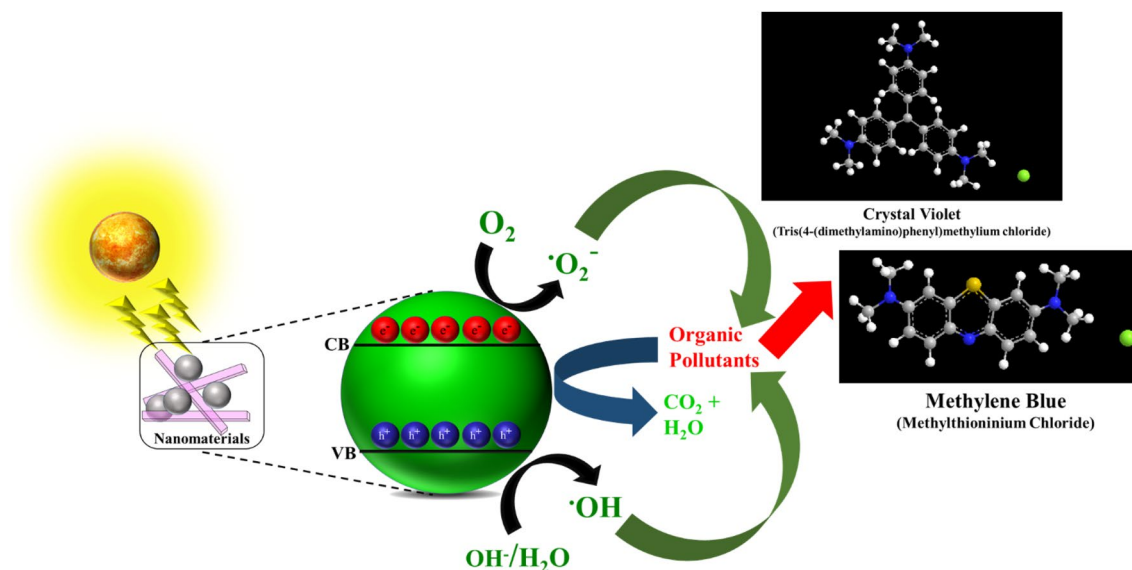

Fig. 18 Mechanistic pathway of dye degradation

confirmed. A colorless solution with an extra absorbance peak at 300 nm denotes the Amino (–NH$_2$) group. When nano-catalyst is added in the reaction system (Fig. 19a), the peak intensity at 400 nm starts decreasing whereas a new absorption peak develops at 300 nm within 390 s. After completion of reaction, almost zero absorbance is at 400 nm, this means solution is completely decolorized. Further we studied the graph of $\ln(A_0/A_t)$ versus time(min.) (Fig. 19b) which gives a straight line passing from the origin with a slope i.e. rate constant (k), where A_0 is the first absorbance value and A_t is the absorbance value at time interval t of the reduction reaction. The calculated value k from the graph is 0.3048 min^{-1}. At 323 and 269 nm, two isosbestic (constant wavelength) points are present, which indicates a (Fig. 19c) clear conversion (i.e. 95%). The Schematic possible chemical reduction reaction is given in (Scheme 1),

Mechanistic pathway of reduction of 4-Nitrophenol reaction

The reduction of 4-NP to 4-AP happens by hydrogenation, with NaBH$_4$ acting as the source of hydrogen. NaBH$_4$ contributes to the ionization of H$^+$ from water. The reduction process happens in two stages: hydrogen atom adsorption and water molecule elimination. A strong repulsive interaction exists between BH$_4^-$ and 4-NP, making the reduction process difficult. The solution of NaBH$_4$ and 4-NP is stable due to electrostatic repulsion between the BH$_4^-$ and 4-NP. Only NaBH$_4$ stabilizes this solution. When NaBH$_4$ is added to water, BH$_4^-$ ions form, and in the case of metal oxides, hydrogen moves from BH$_4^-$ to 4-NP. The hydrogenation catalytic process happens in several ways, depending on the surface quality of the Nanocatalyst. On the metal NPs surface, which works as a Nanocatalyst, electrons move from
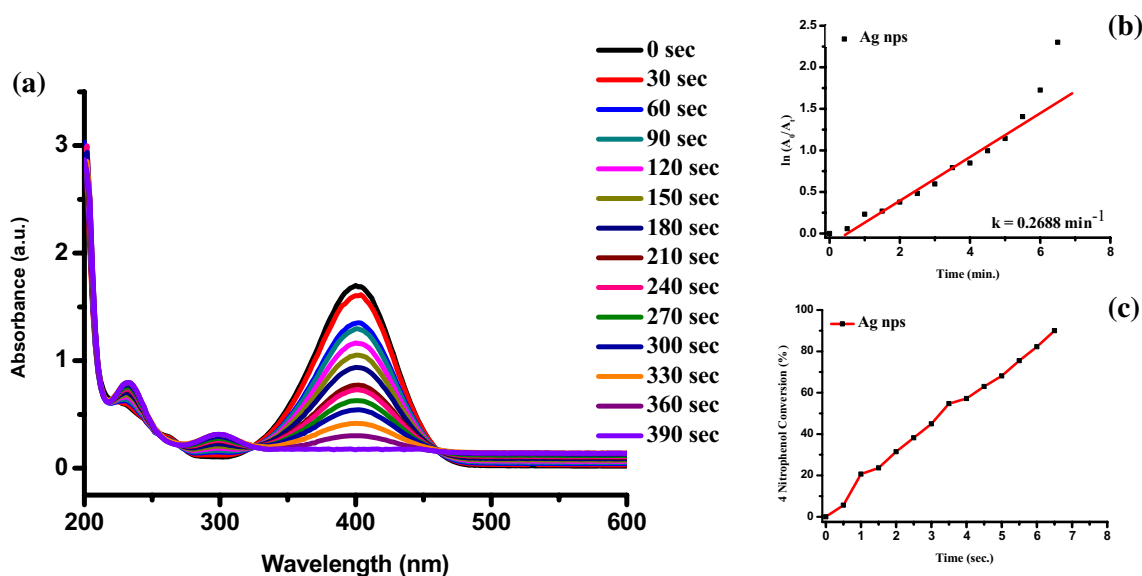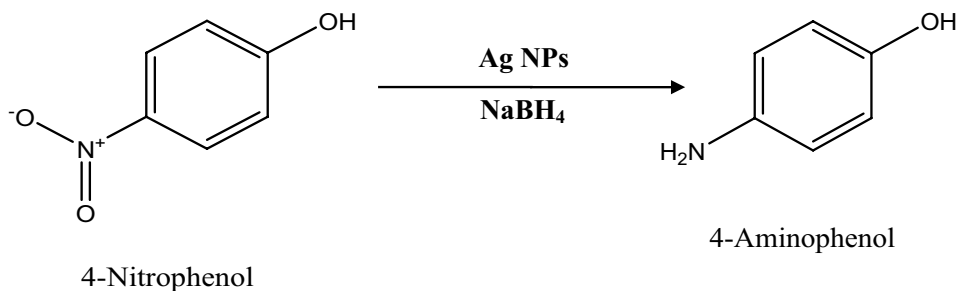

Fig. 19 UV–Vis Spectra indicating **a** reduction of 4-Nitrophenol to 4-Aminophenol with time, **b** Kinetics of catalytic reduction and **c** Percentage conversion of 4-Nitrophenol in the presence of catalyst Ag np's

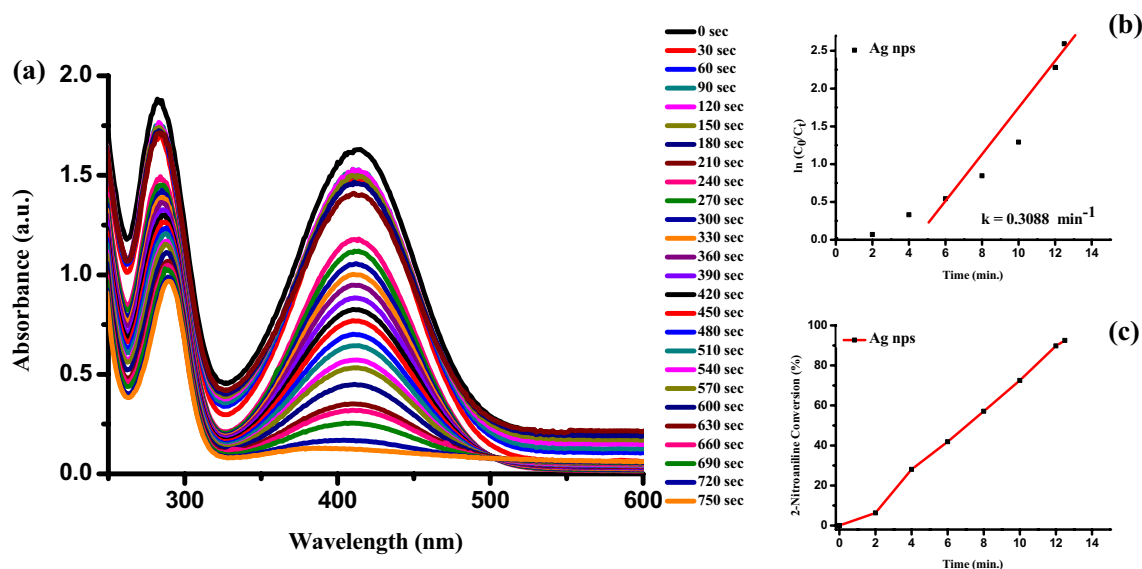**Scheme 1** Conversion of 4-Nitrophenol to 4-Aminophenol in the presence of nano-catalyst

Fig. 20 UV−Vis absorption spectra of **a** 2-Nitroaniline, **b** Kinetics of catalytic reduction and **c** Percentage conversion of 2-Nitroaniline in the presence of catalyst Ag NPs

BH_4^- to 4-NP. The O-atom of 4-NP adsorbs one free hydrogen atom in the Nitro group. The cluster is then joined by another H-atom. This results in a dihydroxyl-like structure. Following that, 4-NP is synthesized by creating and removing one water molecule by hydroxyl dehydration. Finally, 4-AP is produced (Aditya et al. 2017; Kong et al. 2017; Elfiad et al. 2018; Baye et al. 2020; Rawat et al. 2021).

Reduction of nitro-group containing aromatic chemicals

In addition to 4-nitrophenol, many other nitro-groups containing aromatic chemicals are widely used in synthetic organic chemistry. Taking this into consideration, we selected three more nitro group containing organic compounds and studied the catalytic efficacy of the synthesized NPs and nano-composites for organic transformation reactions. The reduction of 2-Nitroaniline (2-NA), 3-Nitroaniline (3-NA) and 4-Nitroaniline (4-NA), over Ag NPs act as Nano-catalyst, was studied with the unaltered conditions. The absorption peak of the Nitro-group containing chemicals is at wavelength 413, 363 and 382 nm for 2-NA, 3-NA and 4-NA, respectively. Catalytic reduction of 2-NA, 3-NA and 4-NA are (Figs. 20a, 21a and 22a) analysed using UV−Vis spectra of the reaction. As the reaction proceeds the peak intensity reduces that indicates the conversion of 2-NA to 2-aminoaniline (2-AP), 3-NA to 3-aminoaniline (3-AP) and 4-NA to 4-aminoaniline (4-AP) it takes 12.5, 13- and 11.5-min. time, resp. for complete conversion. Figures 20b, 21b, and 22b demonstrate the progress of the reaction. Approximately 95, 75, and 98 percent of the reactant is converted into product during this time. The graph

of $\ln(A_0/A_t)$ with time (min) (Figs. 20c, 21c, and 22c) shows that they have a linear relationship. The 2-NA, 3-NA, and 4-NA reduction reactions are examples of first-order reactions with k values of 0.1772, 0.0974, and 0.2519 min^{-1}.

Scheme 2, 3, and 4 give the conversion between 2-NA to 2-AP, 3-NA to 3-AP and 4-NA to 4-AP.

As from earlier reports, the reduction reaction of Nitro-group containing aromatic chemicals occurs at the surface of Nano-catalyst and the mechanism is Nitro-group containing aromatic chemicals and $NaBH_4$ which acts as a reducing agent in the reaction, are attached to the active Nanocatalyst surface.

Conclusions

The effective biogenic synthesis of silver nanoparticles through biogenic routes using Z officinale rhizome extract took place. ZnO nanomaterials are hydrothermally synthesized. Further, we synthesized the nano-composite materials using these two nanomaterials. UV−Vis spectroscopy, XRD, SEM, FE-SEM, Zeta Potential and DLS examinations were used to analyze the size, shape, stability and structure of synthesized nanomaterials. According to zeta potential investigations, nanomaterials, particularly nanocomposites, show exceptional stability without the addition of any external stabilizing agent. These findings show that the NPs produced are mostly spherical, polydisperse, and biocompatible. The synthesized NPs are used as a catalyst for chemical reductions. Herein, we successfully reduced different aromatic compounds containing nitro groups. Further, we tried to
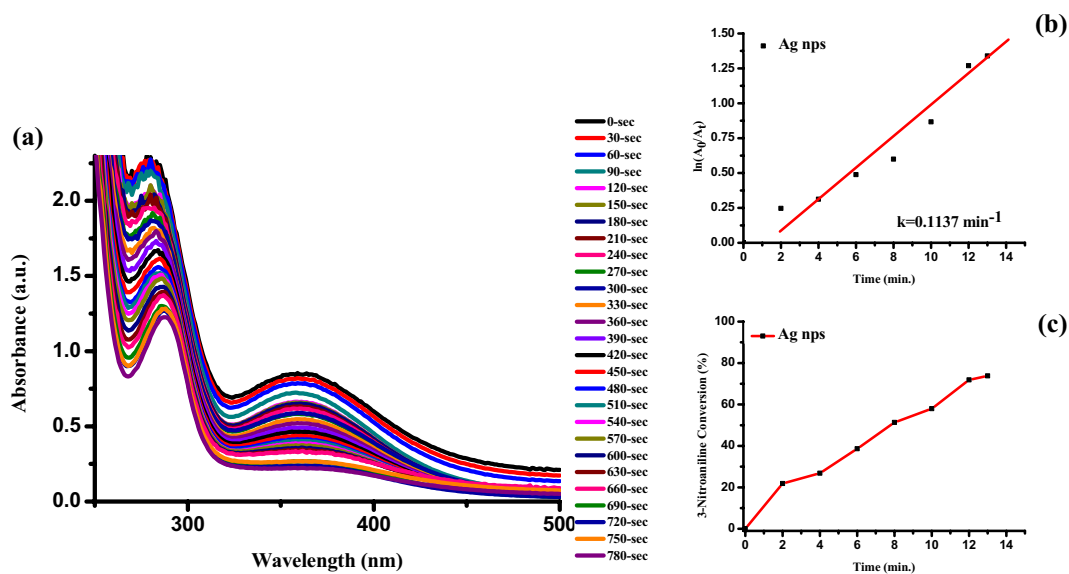
Fig. 21 UV−Vis absorption spectra of **a** 3-Nitroaniline, **b** Kinetics of catalytic reduction and **c** Percentage conversion of 3-Nitroaniline in the presence of catalyst A1g NPs
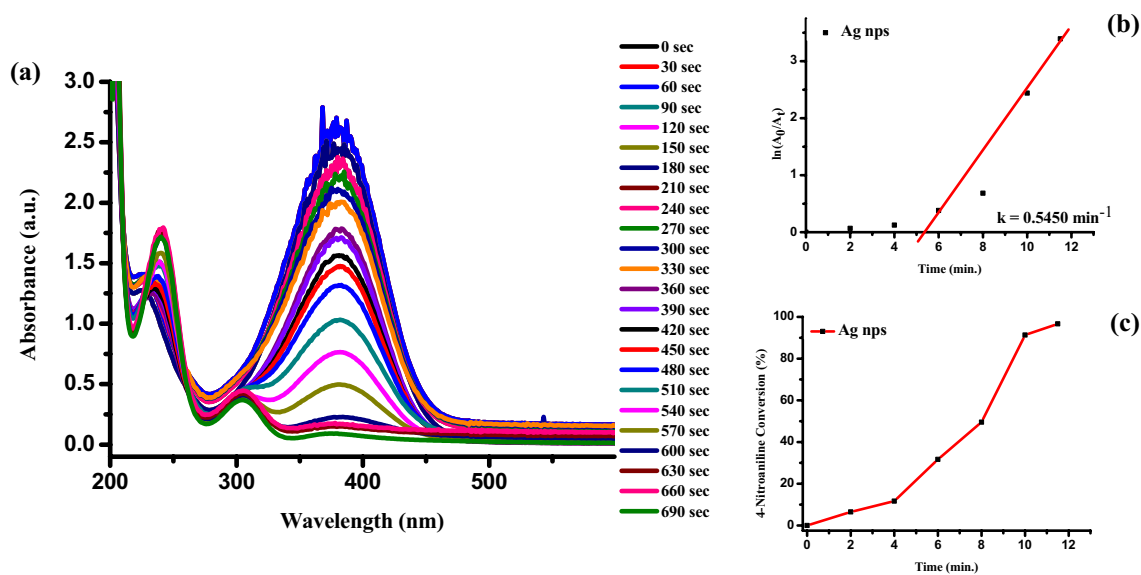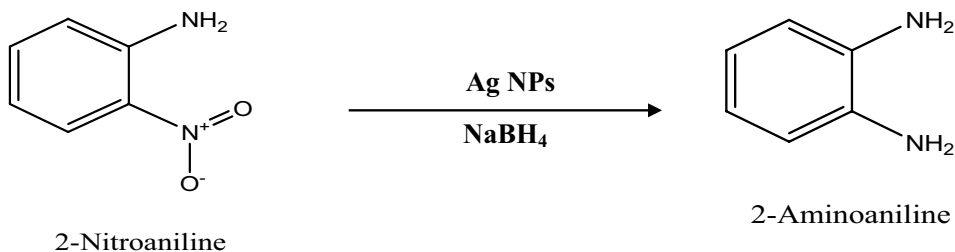

Fig. 22 UV−Vis absorption spectra of **a** 4-Nitroaniline, **b** Kinetics of catalytic reduction and **c** Percentage conversion of 4-Nitroaniline in the presence of catalyst Ag NPs
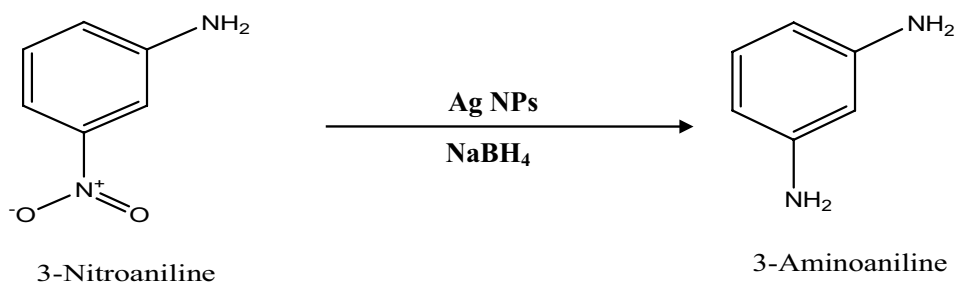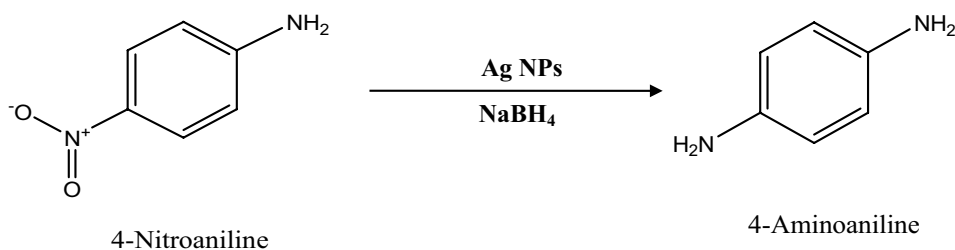
Scheme 2 Conversion of 2-Nitroaniline to 2-Aminoaniline in the presence of nanocatalyst

Scheme 3 Conversion of 3-Nitroaniline to 3-Aminoaniline in the presence of nanocatalyst

Scheme 4 Conversion of 4-Nitroaniline to 4-Aminoaniline in the presence of nanocatalyst

study the catalytic efficacies of ZnO nanorods and nanocomposites of Ag–ZnO, it is observed that ZnO nanorods and the nanocomposites exhibited little catalytic efficacy. We studied the efficacy of synthesized nanomaterials for degradation of organic dyes methylene blue and crystal violet. The current work offers a new route for very convenient and easy-to-commercialize photocatalytic reduction processes.

Declarations

Conflict of interest There is no conflict of interest for the publication of article.

References

Abutalib MM, Rajeh A (2020) Influence of ZnO/Ag nanoparticles doping on the structural, thermal, optical and electrical properties of PAM/PEO composite. Phys B Condens Matter 578:411796. https://doi.org/10.1016/j.physb.2019.411796

Aditya T, Jana J, Singh NK et al (2017) Remarkable Facet Selective Reduction of 4-Nitrophenol by Morphologically Tailored (111) Faceted Cu₂O Nanocatalyst. ACS Omega 2:1968–1984. https://doi.org/10.1021/acsomega.6b00447

Ahmad N, Sharma S, Alam MK et al (2010) Rapid synthesis of silver nanoparticles using dried medicinal plant of basil. Colloids Surfaces B Biointerfaces 81:81–86. https://doi.org/10.1016/j.colsurfb.2010.06.029

Aziz WJ, Jassim HA (2018) A novel study of pH influence on Ag nanoparticles size with antibacterial and antifungal activity using green synthesis. World Sci News 97:139–152

Baruah B, Gabriel GJ, Akbashev MJ, Booher ME (2013) Facile synthesis of silver nanoparticles stabilized by cationic polynorbornenes and their catalytic activity in 4-nitrophenol reduction. Langmuir 29:4225–4234. https://doi.org/10.1021/la305068p

Baye AF, Appiah-Ntiamoah R, Kim H (2020) Synergism of transition metal (Co, Ni, Fe, Mn) nanoparticles and "active support" Fe₃O₄@C for catalytic reduction of 4-nitrophenol. Sci Total Environ 712:135492. https://doi.org/10.1016/j.scitotenv.2019.135492

Beura R, Pachaiappan R, Paramasivam T (2021) Photocatalytic degradation studies of organic dyes over novel Ag-loaded ZnO-graphene hybrid nanocomposites. J Phys Chem Solids 148:109689. https://doi.org/10.1016/j.jpcs.2020.109689

Chanda A, Gupta S, Vasundhara M et al (2017) Study of structural, optical and magnetic properties of cobalt doped ZnO nanorods. RSC Adv 7:50527–50536. https://doi.org/10.1039/c7ra08458g

Chiou JR, Lai BH, Hsu KC, Chen DH (2013) One-pot green synthesis of silver/iron oxide composite nanoparticles for 4-nitrophenol reduction. J Hazard Mater 248–249:394–400. https://doi.org/10.1016/j.jhazmat.2013.01.030

Cui J, Zhang Z, Jiang H et al (2019) Ultrahigh recovery of fracture strength on mismatched fractured amorphous surfaces of silicon carbide. ACS Nano 13:7483–7492. https://doi.org/10.1021/acsnano.9b02658

Deka P, Deka RC, Bharali P (2014) In situ generated copper nanoparticle catalyzed reduction of 4-nitrophenol. New J Chem 38:1789–1793. https://doi.org/10.1039/c3nj01589k

Divband B, Khatamian M, Eslamian GRK, Darbandi M (2013) Synthesis of Ag/ZnO nanostructures by different methods and investigation of their photocatalytic efficiency for 4-nitrophenol degradation. Appl Surf Sci 284:80–86. https://doi.org/10.1016/j.apsusc.2013.07.015

Elfiad A, Galli F, Djadoun A et al (2018) Natural α-Fe2O3 as an efficient catalyst for the p-nitrophenol reduction. Mater Sci Eng B Solid-State Mater Adv Technol 229:126–134. https://doi.org/10.1016/j.mseb.2017.12.009

Gao P, Ng K, Sun DD (2013) Sulfonated graphene oxide-ZnO-Ag photocatalyst for fast photodegradation and disinfection under visible light. J Hazard Mater 262:826–835. https://doi.org/10.1016/j.jhazmat.2013.09.055

Guo Y, Dai M, Zhu Z et al (2019) Chitosan modified Cu₂O nanoparticles with high catalytic activity for p-nitrophenol reduction. Appl Surf Sci 480:601–610. https://doi.org/10.1016/j.apsusc.2019.02.246

Hedberg J, Eriksson M, Kesraoui A et al (2021) Transformation of silver nanoparticles released from skin cream and mouth spray in artificial sweat and saliva solutions: particle size, dissolution, and surface area. Environ Sci Pollut Res 28:12968–12979. https://doi.org/10.1007/s11356-020-11241-w

Huang N, Shu J, Wang Z et al (2015) One-step pyrolytic synthesis of ZnO nanorods with enhanced photocatalytic activity and high photostability under visible light and UV light irradiation. J Alloys Compd. https://doi.org/10.1016/j.jallcom.2015.07.039

Joseph S, Mathew B (2015) Facile synthesis of silver nanoparticles and their application in dye degradation. Mater Sci Eng B Solid-State Mater Adv Technol 195:90–97. https://doi.org/10.1016/j.mseb.2015.02.007

Jyoti K, Baunthiyal M, Singh A (2016) Characterization of silver nanoparticles synthesized using Urtica dioica Linn. leaves and their synergistic effects with antibiotics. J Radiat Res Appl Sci 9:217–227. https://doi.org/10.1016/j.jrras.2015.10.002

Khan Z, Hussain JI, Hashmi AA (2012) Shape-directing role of cetyltrimethylammonium bromide in the green synthesis of Ag-nanoparticles using Neem (Azadirachta indica) leaf extract. Colloids Surfaces B Biointerfaces 95:229–234. https://doi.org/10.1016/j.colsurfb.2012.03.002

Kong X, Zhu H, Le CC et al (2017) Insights into the reduction of 4-nitrophenol to 4-aminophenol on catalysts. Chem Phys Lett 684:148–152. https://doi.org/10.1016/j.cplett.2017.06.049

Kuroda K, Ishida T, Haruta M (2009) Reduction of 4-nitrophenol to 4-aminophenol over Au nanoparticles deposited on PMMA. J Mol Catal A Chem 298:7–11. https://doi.org/10.1016/j.molcata.2008.09.009

Liang X, Chen X, Xiang Z et al (2018) Design and synthesis of surface-controlled CuOₓ/rGO nanocomposites with unusually high efficiency in catalytic conversion of organic reactants in the presence of NaBH₄. Appl Surf Sci 459:716–722. https://doi.org/10.1016/j.apsusc.2018.08.079

Liao L, Zhang Z, Meng F et al (2021) A novel slurry for chemical mechanical polishing of single crystal diamond. Appl Surf Sci 564:150431. https://doi.org/10.1016/j.apsusc.2021.150431

Liu B, Zeng HC (2003) Hydrothermal synthesis of ZnO nanorods in the diameter regime of 50 nm. J Am Chem Soc 125:4430–4431. https://doi.org/10.1021/ja0299452

Liu H, Zhong L, Govindaraju S, Yun K (2019a) ZnO rod decorated with Ag nanoparticles for enhanced photocatalytic degradation of methylene blue. J Phys Chem Solids 129:46–53. https://doi.org/10.1016/j.jpcs.2018.12.040

Liu Y, Zhang Q, Xu M et al (2019b) Novel and efficient synthesis of Ag-ZnO nanoparticles for the sunlight-induced photocatalytic degradation. Appl Surf Sci 476:632–640. https://doi.org/10.1016/j.apsusc.2019.01.137

Mahdieh M, Zolanvari A, Azimee AS, Mahdieh M (2012) Green biosynthesis of silver nanoparticles by Spirulina platensis. Sci Iran 19:926–929. https://doi.org/10.1016/j.scient.2012.01.010

Marimuthu S, Antonisamy AJ, Malayandi S et al (2020) Silver nanoparticles in dye effluent treatment: A review on synthesis, treatment methods, mechanisms, photocatalytic degradation, toxic effects and mitigation of toxicity. J Photochem Photobiol B Biol 205:111823

Meti S, Rahman MR, Ahmad MI, Bhat KU (2018) Chemical free synthesis of graphene oxide in the preparation of reduced graphene oxide-zinc oxide nanocomposite with improved photocatalytic properties. Appl Surf Sci 451:67–75. https://doi.org/10.1016/j.apsusc.2018.04.138

Mukherjee S, Chowdhury D, Kotcherlakota R et al (2014) Potential theranostics application of bio-synthesized silver nanoparticles (4-in-1 system). Theranostics 4:316–335. https://doi.org/10.7150/thno.7819

Nagar N, Devra V (2019) A kinetic study on the degradation and biodegradability of silver nanoparticles catalyzed Methyl Orange and textile effluents. Heliyon 5:e01356. https://doi.org/10.1016/j.heliyon.2019.e01356

Nazeruddin GM, Prasad NR, Prasad SR et al (2014) Coriandrum sativum seed extract assisted in situ green synthesis of silver nanoparticle and its anti-microbial activity. Ind Crops Prod 60:212–216. https://doi.org/10.1016/j.indcrop.2014.05.040

Paulkumar K, Gnanajobitha G, Vanaja M et al (2017) Green synthesis of silver nanoparticle and silver based chitosan bionanocomposite using stem extract of Saccharum officinarum and assessment of its antibacterial activity. Adv Nat Sci Nanosci Nanotechnol. https://doi.org/10.1088/2043-6254/aa7232

Pawar NV, Pai SR, Nimbalkar MS, Dixit GB (2015) RP-HPLC analysis of phenolic antioxidant compound 6-gingerol from in vitro cultures of Zingiber officinale Roscoe. Plant Sci Today 2:24–28

Polsongkram D, Chamninok P, Pukird S et al (2008) Effect of synthesis conditions on the growth of ZnO nanorods via hydrothermal method. Phys B Condens Matter 403:3713–3717. https://doi.org/10.1016/j.physb.2008.06.020

Prasad TNVKV, Elumalai EK (2011) Biofabrication of Ag nanoparticles using Moringa oleifera leaf extract and their antimicrobial activity. Asian Pac J Trop Biomed 1:439–442. https://doi.org/10.1016/S2221-1691(11)60096-8

Prasad RD, Charmode N, Shrivastav OP et al (2021) A review on concept of nanotechnology in veterinary medicine. ES Food Agrofor. https://doi.org/10.30919/esfaf481

Rawat J, Bijalwan K, Negi C et al (2021) Magnetically recoverable Au doped iron oxide nanoparticles coated with graphene oxide for catalytic reduction of 4-nitrophenol. Mater Today Proc 45:4869–4873. https://doi.org/10.1016/j.matpr.2021.01.349

Remita H, Saha A, Sharma GK (2013) Investigation into the catalytic activity of porous platinum nanostructures. Langmuir 29:11431–11439. https://doi.org/10.1021/la401302p

Sahiner N, Karakoyun N, Alpaslan D, Aktas N (2013) Biochar-embedded soft hydrogel and their use in Ag nanoparticle preparation and reduction of 4-nitro phenol. Int J Polym Mater Polym Biomater 62:590–595. https://doi.org/10.1080/00914037.2013.769163

Sang S, Li D, Zhang H et al (2017) Facile synthesis of AgNPs on reduced graphene oxide for highly sensitive simultaneous detection of heavy metal ions. RSC Adv 7:21618–21624. https://doi.org/10.1039/c7ra02267k

Shankar SS, Rai A, Ahmad A, Sastry M (2004) Rapid synthesis of Au, Ag, and bimetallic Au core-Ag shell nanoparticles using Neem (Azadirachta indica) leaf broth. J Colloid Interface Sci 275:496–502. https://doi.org/10.1016/j.jcis.2004.03.003

Suryavanshi RD, Mohite SV, Bagade AA et al (2018) Nanocrystalline immobilised ZnO photocatalyst for degradation of benzoic acid and methyl blue dye. Elsevier, Amsterdam

Suryavanshi RD, Mohite SV, Shaikh SK et al (2018b) Spray deposited Fe2O3 photoelectrode for degradation of benzoic acid and methyl blue dye under solar radiation. J Mater Sci Mater Electron 29:20875–20884. https://doi.org/10.1007/s10854-018-0230-7

Twu YK, Chen YW, Shih CM (2008) Preparation of silver nanoparticles using chitosan suspensions. Powder Technol 185:251–257. https://doi.org/10.1016/j.powtec.2007.10.025

Upadhaya D, Dhar Purkayastha D (2020) Enhanced wettability and photocatalytic activity of seed layer assisted one dimensional ZnO nanorods synthesized by hydrothermal method. Ceram Int 46:15831–15839. https://doi.org/10.1016/j.ceramint.2020.03.130

Vinila VS, Jacob R, Mony A et al (2014) XRD studies on nano crystalline ceramic superconductor PbSrCaCuO at different treating

temperatures. Cryst Struct Theory Appl 03:1–9. https://doi.org/10.4236/csta.2014.31001

Wu Z, Xu C, Wu Y et al (2013) ZnO nanorods/Ag nanoparticles heterostructures with tunable Ag contents: a facile solution-phase synthesis and applications in photocatalysis. CrystEngComm 15:5994–6002. https://doi.org/10.1039/c3ce40753e

Yeh H, Chuang C, Chen H et al (2014) Bioactive components analysis of two various gingers (Zingiber officinale Roscoe) and antioxidant effect of ginger extracts. LWT - Food Sci Technol 55:329–334. https://doi.org/10.1016/j.lwt.2013.08.003

Zhang Z, Su H (2020) Green chemical mechanical polishing of sapphire wafers using a novel slurry. Nanoscale 12:22518–22526. https://doi.org/10.1039/d0nr04705h

Zhang P, Shao C, Zhang Z et al (2011) In situ assembly of well-dispersed Ag nanoparticles (AgNPs) on electrospun carbon nanofibers (CNFs) for catalytic reduction of 4-nitrophenol. Nanoscale 3:3357–3363. https://doi.org/10.1039/c1nr10405e

Zhang Z, Wang B, Kang R et al (2015) Changes in surface layer of silicon wafers from diamond scratching. CIRP Ann - Manuf Technol 64:349–352. https://doi.org/10.1016/j.cirp.2015.04.005

Zhang Z, Cui J, Wang B et al (2017) AC SC. J Alloys Compd. https://doi.org/10.1016/j.jallcom.2017.08.024

Zhang X, Sun H, Tan S et al (2019) Hydrothermal synthesis of Ag nanoparticles on the nanocellulose and their antibacterial study. Inorg Chem Commun 100:44–50. https://doi.org/10.1016/j.inoche.2018.12.012

Zhang Z, Wang X, Meng F et al (2022) Origin and evolution of a crack in silicon induced by a single grain grinding. J Manuf Process 75:617–626. https://doi.org/10.1016/j.jmapro.2022.01.037

Zhao Y, Jiang Y, Fang Y (2006) Spectroscopy property of Ag nanoparticles. Spectrochim Acta - Part A Mol Biomol Spectrosc 65:1003–1006. https://doi.org/10.1016/j.saa.2006.01.010

Zhenyu Z, Fengwei H, Xianzhong Z, Dongming G (2012) Fabrication and size prediction of crystalline nanoparticles of silicon induced by nanogrinding with ultrafine diamond grits. Scr Mater 67:657–660